Title: Fatty acid amide hydrolase gene inactivation induces hetero-cellular potentiation of microglial function in the 5xFAD mouse model of Alzheimer's disease

Running title: FAAH inactivation boosts microglia in 5xFAD

Authors: María Andrea Arnanz[1], María Ferrer[2], María Teresa Grande[1], Samuel Ruiz de Martín Esteban[1], Gonzalo Ruiz-Pérez[3], Benjamin F. Cravatt[4], Ricardo Mostany[5], Víctor Javier Sánchez-Arévalo Lobo[1,2], Julián Romero[1*] and Ana María Martínez-Relimpio[1*].

Affiliations:

[1]Faculty of Experimental Sciences, Universidad Francisco de Vitoria, 28223, Pozuelo de Alarcón, Madrid, Spain

[2]Departamento de Anatomía Patológica, Instituto de Investigación Hospital 12 de Octubre, Av. Córdoba, s/n, 28041 Madrid, Spain

[3]Neuroscience Research Center and Department of Pharmacology and Toxicology, Medical College of Wisconsin, Milwaukee, Wisconsin, USA

[4] The Skaggs Institute for Chemical Biology and Departments of Cell Biology and Chemistry, The Scripps Research Institute, La Jolla, San Diego, CA, 92037, USA

[5]Department of Pharmacology, Tulane University School of Medicine, New Orleans, LA, 70112, USA

Corresponding authors: Julián Romero, PhD (j.romero.prof@ufv.es; https://orcid.org/0000-0002-2897-606X) and Ana María Martínez-Relimpio, PhD (am.martinez.prof@ufv.es; https://orcid.org/0000-0001-8432-937X).

Word count: 10053 words

Title: Fatty acid amide hydrolase gene inactivation induces hetero-cellular potentiation of microglial function in the 5xFAD mouse model of Alzheimer's disease

Authors: María Andrea Arnanz[1], María Ferrer[2], María Teresa Grande[1], Samuel Ruiz de Martín Esteban[1], Gonzalo Ruiz-Pérez[3], Benjamin F. Cravatt[4], Ricardo Mostany[5], Víctor Javier Sánchez-Arévalo Lobo[1,2], Julián Romero[1*] and Ana María Martínez-Relimpio[1*].

Affiliations:

[1]Faculty of Experimental Sciences, Universidad Francisco de Vitoria, 28223, Pozuelo de Alarcón, Madrid, Spain

[2]Departamento de Anatomía Patológica, Instituto de Investigación Hospital 12 de Octubre, Av. Córdoba, s/n, 28041 Madrid, Spain

[3]Neuroscience Research Center and Department of Pharmacology and Toxicology, Medical College of Wisconsin, Milwaukee, Wisconsin, USA

[4] The Skaggs Institute for Chemical Biology and Departments of Cell Biology and Chemistry, The Scripps Research Institute, La Jolla, San Diego, CA, 92037, USA

[5]Department of Pharmacology, Tulane University School of Medicine, New Orleans, LA, 70112, USA

Corresponding authors: Julián Romero, PhD (j.romero.prof@ufv.es; https://orcid.org/0000-0002-2897-606X) and Ana María Martínez-Relimpio, PhD (am.martinez.prof@ufv.es; https://orcid.org/0000-0001-8432-937X).

DATA AVAILABILITY STATEMENT

The datasets generated and/or analyzed during the current study are available in the Gene Expression Omnibus (GEO) database, with the accession number SUB14399624 (https://www.ncbi.nlm.nih.gov/geo/).

FUNDING

Funded by Ministerio de Ciencia e Innovación – Agencia Estatal de Investigación and Fondo Europeo de Desarrollo Regional (PID2022-138461OB-I00, supported by MCIN /AEI /10.13039/501100011033 / FEDER, UE) and by Universidad Francisco de Vitoria (UFV2024- 09).

CONFLICT OF INTEREST DISCLOSURE

All authors declare that they have no conflicts of interest.

ETHICS APPROVAL STATEMENT

The animal study was reviewed and approved by Universidad Francisco de Vitoria.

PATIENT CONSENT STATEMENT

Not applicable

PERMISSION TO REPRODUCE MATERIAL FROM OTHER SOURCES

Not applicable

CLINICAL TRIAL REGISTRATION

Not applicable

ABSTRACT

Neuroinflammation has recently emerged as a crucial factor in Alzheimer´s Disease (AD) etiopathogenesis. Microglial cells play an important function in the inflammatory response; specifically, the emergence of disease-associated microglia (DAM) has offered new insights into the conflicting perspectives on the detrimental or beneficial roles of microglia. We previously showed that modulating the endocannabinoid tone by fatty acid amide hydrolase (FAAH) inactivation renders beneficial effects in an amyloidosis context, paradoxically accompanied by an exacerbated neuroinflammatory response and the enrichment of DAM population. Here, we aim to elucidate the role of microglial cells in FAAH-lacking mice in the 5xFAD mouse model of AD by using RNA-sequencing analysis, molecular determinations, and morphological studies by using *in vivo* multiphoton microscopy. FAAH-lacking AD mice displayed upregulated inflammatory genes and exhibited a DAM genetic profile. Conversely, genes linked to AD were downregulated. Depleting microglia using PLX5622 revealed that plaque-associated microglia in FAAH-deficient AD mice had a more stable, ramified morphology and increased Aβ uptake, leading to reduced plaque growth compared to control mice. Importantly, FAAH expression was negligible in microglial cells, thus suggesting a role for FAAH in the cellular interplay in the central nervous system. Our findings show that *Faah* gene inactivation triggers a hetero-cellular enhancement of microglial function that was paradoxically paralleled by an exacerbated inflammatory response. Taken together, the present data highlight FAAH as a potential therapeutic target in AD.

Keywords

Alzheimer´s disease, fatty acid amide hydrolase, neuroinflammation, microglia, damage associated microglia, two-photon microscopy.

Main Points:

- 5xFAD/FAAH$^{-/-}$ mice exhibit upregulated inflammatory genes, DAM profile, and downregulated AD-linked genes.
- Microglia in 5xFAD/FAAH$^{-/-}$ mice have ramified morphology and increased Aβ uptake.
- FAAH inactivation enhances microglial function in 5xFAD.

INTRODUCTION

Alzheimer's disease (AD) is a neurodegenerative disorder characterized by the deterioration of cognitive functions and changes in behavior, typically beginning with impaired short-term memory. It has become the leading cause of dementia and its worldwide prevalence is projected to continue rising. AD is considered a multifactorial disorder influenced by various risk factors such as advancing age, vascular diseases, and genetic factors that significantly contribute to disease development (1). From a molecular point of view, primary changes include intraneuronal deposits of hyperphosphorylated tau protein (so called “neurofibrillary tangles”), reduced levels of acetylcholinesterase, and formation of extracellular deposits of amyloid beta (Aβ) peptide 1-42 and 1-40 in the brain parenchyma (referred to as “neuritic plaques”) (1). However, accumulating evidence suggests that these classic pathological hallmarks cannot fully explain much of the pathogenesis of AD, suggesting the involvement of additional mechanisms of disease. Specifically, with the discovery of elevated levels of inflammatory markers in AD patients, inflammation has emerged as a crucial factor in AD etiopathogenesis (2).

Neuroinflammation generally refers to an inflammatory response within the central nervous system (CNS) and is a common feature in the development of neurodegenerative pathologies. It can be considered as a physiological protective response that, when chronically active, can also drive neurodegeneration. Nevertheless, the role played by neuroinflammation in neurodegenerative diseases, particularly in AD, is still a subject of debate (2). In general, it is accepted that there is a significant chronic release of inflammatory cytokines in the AD brain, primarily from microglial cells. Microglia, the resident macrophages of the brain and spinal cord,

have traditionally been described as a uniform population of cells, essential for CNS development and brain homeostasis. However, under neurodegenerative conditions, they transition from their normal function to a state where they become detrimental to CNS health (3). Recently, comprehensive single-cell RNA analysis of CNS immune cells under neurodegenerative conditions has revealed the existence of disease-associated microglia (DAM) (4). These microglia represent a distinct subset of cells displaying a unique transcriptional and functional signature. In AD mouse models, DAM are closely associated with Aβ plaques, participate in the clearance of amyloid peptides, and exhibit defined gene expression profiles characterized by reduced expression of homeostatic microglial genes (4). The emergence of DAM as significant contributors to brain diseases offers new insights into the conflicting perspectives on the detrimental or beneficial roles of microglia. However, further research is required to understand the triggering mechanisms, signaling pathways, and regulatory checkpoints associated with DAM, as well as their implications in various brain diseases (5). In this way, developing strategies focused on modulating microglial function, such as molecules targeting the colony stimulating factor-1 receptor (CSF1R), are emerging, not only as a novel approach to treat neurodegenerative diseases, but also to explore the contribution of microglia to AD progress in the initial stages of the disease (6,7).

The endocannabinoid system (ECS) plays an important role in the regulation of CNS homeostasis by participating in several key functions, including neurotransmission, inflammation, as well as neuronal and glial cell proliferation, differentiation, migration, and survival (8). The ECS is composed of endogenous cannabinoids, cannabinoid receptors, and the enzymes responsible for the synthesis and degradation of endocannabinoids. In recent years, there has been a growing interest in studying the role of the ECS in health and disease, and some of its components are now considered as potential pharmacotherapeutic targets for different conditions (9). Specifically, the ECS appears to be relevant as a therapeutic target in

149 neurodegenerative diseases such as Parkinson's disease, epilepsy, AD, and amyotrophic lateral
150 sclerosis.

151 The modulation of the ECS by increasing the endocannabinoid tone appears to be a promising
152 strategy for the treatment of various CNS diseases. Specifically, the inhibition of
153 endocannabinoids' catabolic enzyme fatty acid amide hydrolase (FAAH) has been suggested as a
154 putative therapeutic approach (10). FAAH is the main degradative enzyme for anandamide (AEA),
155 as well as other N-acylethanolamines (NAEs), such as N-oleoylethanolamine and N-
156 palmitoylethanolamine. Pharmacological inactivation of FAAH leads to heightened
157 endocannabinoid neurotransmission and may counteract neuroinflammation, pain, depression
158 and anxiety (11). Consequently, FAAH represents a promising therapeutic target for various
159 disorders affecting the peripheral and CNS and several FAAH inhibitors are currently being tested
160 in clinical trials. One of them is Pfizer's PF-04457845, a highly potent and selective FAAH inhibitor,
161 which is currently under investigation for treating post-traumatic stress disorders and Tourette's
162 syndrome, among others (11). In the case of AD, it is speculated that elevated FAAH expression
163 levels in the brain correlate with reduced levels of lipid amides and with an increase in
164 symptomatology (12). Therefore, FAAH enzyme inhibition shows promising potential for
165 improving symptoms associated with AD (12,13).

166 Previous data from our group revealed that the genetic inactivation of *Faah* leads to a significant
167 modification of the inflammatory state in the mouse brain, characterized by an increased
168 expression of proinflammatory cytokines. Paradoxically, this enhanced neuroinflammatory
169 milieu has beneficial consequences in terms of prevention of memory impairment, synaptic
170 plasticity, and decreased amyloid peptide deposition (14–17). Although the expression of FAAH
171 is mainly located in neurons and reactive astrocytes (18,19), these results suggest that this pro-
172 inflammatory environment might induce a shift in the activity and inflammatory profile of
173 microglial cells. This was evident, for instance, in the increased microglial ability to respond

against a laser-induced acute injury to the brain parenchyma (15). Furthermore, the microglia M1/M2 ratio in mice lacking FAAH activity was significantly elevated and accompanied by a decrease in microgliosis and amyloid peptide levels (16). Finally, we also showed that microglia of FAAH-deficient mice have a greater capacity to phagocytose Aβ and show a profile closer to that of DAM (14). Therefore, these observations seem confirmative of the role of FAAH in the control of the inflammatory status of the mouse brain and underline the relevance of microglial cells as key players in these effects.

The present work aims to define the molecular and morphological profiles of microglia following the genetic inactivation of *Faah* in the context of AD. To achieve this goal, we have performed a transcriptomic analysis and quantified the expression levels of several parameters indicative of the microglial activational state in 5xFAD mice. Additionally, we carried out an *in vivo* multiphoton microscopy study to analyze the impact of *Faah* gene inactivation on microglial morphology as well as on the structural features of neuritic plaques. Since CSF1R inhibitors are useful tools to explore the contribution of microglia to the progression of AD, we also induced the pharmacological ablation of microglial cells with PLX5622, and subsequent repopulation, to assess whether the genetic inactivation of *Faah* may induce changes in microglial morphology and plaque evolution in the context of AD.

METHODS

Mice

Mice used in these experiments were described in our previous works (14,16,20). Briefly, mice co-expressing five familial Alzheimer's disease mutations in heterozygosis (5xFAD) were purchased from Jackson Laboratories (Bar Harbor, ME, USA) (21) Mice homozygous for disruption of the gene that encodes FAAH were generated by Dr. Cravatt ($FAAH^{-/-}$ mice, (22)) in the C57BL/6 J background by replacing the first FAAH exon (encoding amino acids 1–65) and ≈2

kb of upstream sequence, and, consequently, the functionality of FAAH enzyme was constitutively altered. Then, these mice were crossed with 5xFAD mice and backcrossed for at least 10 generations to generate 5xFAD and 5xFAD/FAAH$^{-/-}$ littermates and their respective WT were used as controls. For experiments involving *in vivo* imaging, the Cx3cr1^{EGFP} mouse line was used to visualize microglia (23). Therefore, 5xFAD and 5xFAD/FAAH$^{-/-}$ mice were mated with Cx3cr1^{EGFP} mice to obtain 5xFAD/Cx3cr1$^{GFP/+}$ and 5xFAD/FAAH$^{-/-}$/Cx3cr1$^{GFP/+}$ mice for *in vivo* imaging of microglia. Mice were housed at the animal facility of Universidad Francisco de Vitoria (authorization number #281150000013). Food and water were available *ad libitum*, and cages were kept under a 12-h light/dark cycle. Experimental protocols met the European and Spanish regulations for protection of experimental animals (2010/63/EU and RD 1201/2005 and 53/2013) and were authorized by the local ethics committee (PROEX149/18).

Transcriptomic analysis

Here we profiled the transcriptome of hippocampi obtained from the brains of 5xFAD and 5xFAD/FAAH$^{-/-}$ using RNA-sequencing (RNA-seq). For tissue collection, six-month-old male (N=3 per genotype) were sacrificed by cervical dislocation and their brains were dissected to obtain hippocampi. Tissues were flash frozen in liquid nitrogen and stored at -80°C until further processing. RNA from hippocampi was isolated with the RNeasy mini kit (Qiagen). Samples were analyzed by using the NovaSeq 6000 sequencing platform (Macrogen). Quality checks on the raw sequencing data were performed using FastQC (version 0.11.9) to ensure data integrity before further processing. Subsequently, we employed Trim Galore (version 0.6.10) for adaptor trimming and removal of low-quality reads. The high-quality trimmed reads were aligned to the mm39 reference genome using the STAR aligner (version 2.7.10b) (24). To quantify gene-level expression, we utilized FeatureCounts from the Subread R package (version 2.01) (25), obtaining expected count data for subsequent analysis. Comparative analysis of expression profiles across different conditions was conducted using the DESeq2 package (version 1.38.0)(26). This analysis

224 employs a model based on a negative binomial distribution to identify differentially expressed
225 genes. P-values were corrected for multiple testing using the Benjamini-Hochberg False
226 Discovery Rate (FDR) method. Adjusted p-values below 0.05 were considered statistically
227 significant and were used as the basis for functional enrichment analysis and Gene Set
228 Enrichment Analysis (GSEA). GSEA was carried out with the GSEAPy Python package (27). We
229 analyzed the expression data against a compendium of gene sets that represent Hallmark and
230 the Kyoto Encyclopedia of Genes and Genomes (KEGG) pathways. Gene sets for the GSEA were
231 sourced from the Molecular Signatures Database (MSigDB version 7.0) (28). To enhance the
232 robustness of our findings, we performed 1,000 gene-set permutations during the GSEA. Terms
233 with both FDR-adjusted $p<0.05$ and a nominal p value < 0.05 were deemed statistically
234 significant.

235 **Molecular determinations**

236 The expression of genes and molecules associated with the intrinsic activity of microglial cells
237 was quantified in order to analyze possible differences due to the genetic inactivation of the
238 FAAH enzyme in the context of AD. Additionally, these molecular determinations were also
239 performed after the treatment of mice with PLX5622, a CSF1R antagonist, provided by Plexxikon
240 Inc. and formulated in AIN-76A standard chow (Research Diets Inc) at 1200 mg/kg that was
241 administered to cause the pharmacological ablation of microglial cells (6). To that end, six-
242 month-old male WT, WT/FAAH$^{-/-}$, 5xFAD and 5xFAD/FAAH$^{-/-}$ mice (N=8 per genotype) were
243 exposed to control or PLX5622 diet *ad libitum* for 4 weeks to cause the pharmacological ablation
244 of microglia. Then, mice were sacrificed and their brains were dissected to obtain hippocampus
245 and cortex, which were processed for qPCR and western blot analysis, respectively.

246 *Quantification of mRNA levels by RT-qPCR*

247 RNA from hippocampus was isolated using Tripure isolation reagent (Roche). Then, a Transcriptor
248 First Strand cDNA Synthesis Kit (Roche) was used according to manufacturer's specifications and

relative gene expression was measured using CFX ConnectTM Real-Time System (Bio-Rad), Quantimix Easy probes Kit (Biotools), and the following mouse probes conjugated with FAM fluorophore PrimePCR™ Probe Assay (Bio-Rad): *Rps18* (qMmuCEP0053856), *Tlr4* (qMmuCIP0035732), *Nlrp3* (qMmuCIP0031558), *Csf1r* (qMmuCEP0054028), *Csf1l* (qMmuCIP0032398), *Il1α* (qMmuCIP0030741), *Il1b* (qMmuCEP0054181) *Cnr2* (Custom) and *Faah* (qMmuCEP0055480). RNA expression was calculated using the comparative Ct method normalized to 18S ribosomal subunit. Data were expressed relative to a calibrator using the $2^{-(\Delta\Delta Ct)} \pm s$ formula.

Protein quantification by western blot

Cortices were homogenized in lysis buffer (MLB: 25mM HEPES, pH 7.5, 150mM NaCl, 1% Igepal CA-630, 10 mM $MgCl_2$, 1mM EDTA, 10% glycerol, 1mM Na_3VO_4, 25mM NaF and protease inhibitor cocktail; Roche). Then, samples were centrifuged at 12,000 xg for 20 min at 4°C and protein concentrations were quantified (BCA Protein Assay Kit, Thermo Scientific). Tissue lysates (50 µg/lane) were loaded into SDS-polyacrylamide gels, and the proteins were transferred onto nitrocellulose membranes (BioRad). After blocking in 5% bovine serum albumin in TTBS (10 mM Tris pH 7.5, 150mM NaCl, 0.1% Tween 20) membranes were incubated overnight at 4°C, as appropriate, with primary antibodies: anti-IBA1 (1:1000 FUJIFILM Wako), anti-CSF1R (1:1000, Abcam), and anti-GAPDH (1:10,000, Abcam). Membranes were incubated with corresponding horseradish peroxidase-conjugated mouse secondary antibody (1:10,000) or anti-rabbit (1:5,000) and were developed using a chemiluminescent reagent (GE Healthcare). Developed signals were recorded on ChemiDoc Imaging System (Bio-Rad) for densitometric analysis (ImageJ).

In vivo imaging experiments

Cranial window surgery

Six-month-old male 5xFAD/Cx3cr1$^{GFP/+}$ and 5xFAD/FAAH$^{-/-}$/Cx3cr1$^{GFP/+}$ mice (N=7-8 per group) were used for intravital analysis of microglia and amyloid plaques using two-photon microscopy. To that end, these mice underwent surgery to implant a chronic glass-covered cranial window over the left barrel cortex as described by Mostany and Portera-Cailliau (29). Mice were anesthetized with a combination of isoflurane (Isoflurin®, 1000 mg/g, Fatro Iberica) and oxygen at 4%, with subsequent maintenance at 1.5% during the surgical procedures under sterile conditions. Animal's core temperature was maintained at 37°C using a heating pad and their eyes were lubricated with eye ointment. Prior to the surgical intervention, dexamethasone (Cortexonavet®, 2 mg/ml, Syva) and carprofen (Norocarp®, 50 mg/ml, Karizoo) were administered subcutaneously and, when the skull was exposed, a drop of lidocaine and epinephrine solution (Anesvet®, 20/0.02 mg/ml, Ovejero Laboratorios) was applied for topical analgesia. The craniotomy (4 mm in diameter) was performed using a pneumatic dental drill, a 5 mm coverslip was placed on top of the dura mater and was secured, as well as a titanium bar, with cyanoacrylate-based glue and dental acrylic (Ortho-Jet® Liquid, Lang Dental).

Chronic in vivo 2PE imaging

All mice were allowed to recover for 4 weeks prior to imaging experiments. After this period, mice received an intraperitoneal dose of methoxy-XO4 to stain amyloid plaques (10 mg/kg, Tocris Bioscience) and, 24 h later, the first imaging session was performed (t=0) to identify both microglial cells and amyloid plaques (at least 3 plaques per mouse and field, two/three fields per mouse) for subsequent tracking. Prior to the imaging acquisition, mice were anesthetized with isoflurane (5.0% for induction, 1 to 1.5% for imaging) and head-fixed to the microscope stage using the titanium bar. Imaging was done using a custom-built two-photon microscope with a femtosecond laser (Chameleon Ultra II, Coherent, Inc.). A 40x 0.8 NA water-immersion objective (Olympus), and ScanImage 3.8 Software written in MATLAB (Mathworks; RRID:SCR_001622). Microglial imaging was performed at 950 nm, later switched to 720 nm for visualizing amyloid

plaques to distinguish between microglial subtypes. Low magnification (0.36 µm/pixel) image stacks consisting of 100 single images (512 x 512 pixels) taken at 2 µm intervals (Z-step) were obtained starting approximately 40-50 µm below the brain's surface. Additionally, for a more detailed characterization of amyloid plaques, high magnification (0.18 µm/pixel) image stacks (512 x 512 pixels) taken at 1 µm intervals (Z-step) were captured until the entire plaque was visualized.

After the first imaging session (t=0), PLX5622 treatment was started for 28 consecutive days, followed by exposure to control diet again for 9 days to evaluate cellular repopulation. Methoxy-XO4 i.p injections and image acquisition sessions were repeated at the end of PLX5622 treatment (t=28) and after the repopulation period (t=37). All the images obtained were processed using Imaris software.

3D Reconstruction and microglial morphology analysis

Three-dimensional reconstruction of two-photon microscopy images was performed using Imaris Software (V.10.0, Oxford Instruments). Microglial cells and amyloid plaques were visualized by merging images captured at 950 nm and 720 nm wavelength. An important aspect of microglial morphology analysis was the identification of different microglial subtypes. For this purpose, the Surface tool was used to render amyloid plaques and reconstruct microglial soma. Microglial soma located less than 20 µm from amyloid plaques were classified as plaque-associated microglia, while those situated further than 20 µm were referred to as non-plaque-associated microglia (Supplementary Material Fig. S1). Microglial soma located within 10 µm from the image edges were excluded from the analysis to ensure the rendering of the complete cell structure. To improve image quality, the *Attenuation Correction Extension* of Imaris Software was employed to equalize image brightness throughout the Z-stack. Additionally, microglial processes were modelled using the Imaris *Filament* tool. The number of microglial X04-positive cells was determined using the *Spots* tool and expressed as the percentage of the total number

of microglial cells in each area. The analysis of microglial soma focused on measuring volume and sphericity, while the analysis of microglial processes included total length, sphericity, ramification index, and Sholl analysis. Amyloid plaque analysis involved measuring volume, sphericity, protein density, and intensity standard deviation. Additional details on the object segmentation algorithms used are provided in the Supplementary Material (Fig.S2).

Statistical analysis

The statistical analysis was performed with GraphPad 10.0. Data were analyzed by two-way-anova (followed by Sidak's post-hoc test). All data are expressed as mean ± standard error of the mean (SEM). A p-value <0.05 was considered as statistically significant. The number of mice used in each experiment are included in the figure legends.

RESULTS

Transcriptomic analysis of 5xFAD/FAAH$^{-/-}$ mice revealed a significant enrichment in "Inflammatory Response" pathway and DAM signature, as well as a significant downregulation of "Alzheimer's Disease" pathway.

In our study, RNA-seq analysis of hippocampi obtained from the brains of 5xFAD and 5xFAD/FAAH$^{-/-}$ mice was employed to investigate the transcriptomic alterations stemming from FAAH inactivation in AD context. We undertook differential gene expression analysis, the results of which are depicted in a Volcano plot that delineates genes significantly upregulated (red) and downregulated (blue) with an FDR-adjusted p-value below 0.05, compared to those without significant changes (grey) (Fig. 1A, Supplementary Material Table S3 and Additional material). Pathway enrichment analysis, leveraging Hallmark gene sets and KEGG pathways, unveiled biological processes that are modulated due to FAAH inactivation, as indicated by the Normalized Enrichment Scores (NES). These pathways are associated with a variety of immune

responses, including TNFα, IL-6, and IFN signaling (Fig. 1B). Gene Set Enrichment Analysis (GSEA) revealed a significant enrichment in the “Inflammatory Response” pathway (Fig. 1B, 1D and Supplementary Material Fig. S4A and S4B), and a specific microglia signature from Grubman et al. (30) (Fig. 1F and Supplementary Material Fig. S4C), while the “Alzheimer's Disease” (Fig. 1C, 1E and Supplementary Material Fig. S4B) pathway demonstrated an inverse trend (Fig. 1C and 1E).

Faah **gene inactivation altered the expression pattern of genes associated with microglial function in AD.**

We analyzed the expression of some genes known to be involved in the Aβ-induced activation of microglia to detect possible differences due to the genetic inactivation of FAAH enzyme. We performed RT-qPCR experiments to measure mRNA levels of toll-like receptor 4 (*Tlr4*), NOD-like receptor protein 3 *(Nlrp3)*, *Il1α*, *Il1β*, colony stimulating factor 1 receptor (*Csf-1r*) and its ligand (*Csf1l*), cannabinoid receptor subtype 2 (Cb_2r), and FAAH in WT groups (CTRL and $FAAH^{-/-}$) and AD animals (5xFAD and 5xFAD/$FAAH^{-/-}$) (Fig. 2). As expected, the expression of all genes was significantly increased in AD animals compared to WT groups, except for that of *Faah*, which was significantly reduced. Additionally, expression levels of *Nlrp3, Il1β*, and *Csf1r* were significantly upregulated, while *Csf1l* and Cb_2r were significantly downregulated in 5xFAD/$FAAH^{-/-}$ mice compared to 5xFAD littermates.

Microglial ablation with PLX5622 revealed a FAAH-mediated differential response in the context of AD.

Then, we analyzed tissue samples obtained from 5xFAD and 5xFAD/$FAAH^{-/-}$ mice treated with PLX5622 or control diet for 28 days. This CSF1R-selective antagonist triggers apoptosis in

371 microglial cells, thus allowing for a precise evaluation of putative changes after microglial
372 deletion. To corroborate the ablating effects of PLX5622 on microglia, we first analyzed IBA1 and
373 CSF1R protein levels in cerebral cortex lysates by western blot (Fig. 3A and 3B). As expected, IBA1
374 and CSF1R protein levels were reduced after PLX5622 exposure, regardless of FAAH expression.
375 Interestingly, we observed that CSF1R protein levels were significantly higher in 5xFAD/FAAH$^{-/-}$
376 mice compared to 5xFAD control mice, even though 5xFAD/FAAH$^{-/-}$ control mice exhibited a
377 significant decrease in Iba1 expression (Fig. 3A and 3B). This observation suggests a combined
378 decrease in microgliosis together with an enhanced level of CSF1R expression. Finally, we also
379 assessed whether PLX5622 induced changes in mRNA levels of the same genes previously
380 examined (Fig. 3: 3C to 3J). As expected, *Faah* expression remained unaffected by microglial
381 ablation (Fig. 3J) and the expression of *Tlr4, Nlrp3, Csf1r*, and *Il1α* was significantly reduced after
382 treatment (Fig. 3C, 3D, 3G and 3E, respectively), irrespective of FAAH enzyme inactivity. *Il1β* and
383 *Cb$_2$R* mRNA levels were significantly decreased following microglial ablation in 5xFAD/FAAH$^{-/-}$
384 mice but not in 5xFAD mice (Fig. 3F and 3H, respectively), in which the expression of *Csf1l* was
385 significantly reduced after treatment (Fig. 3I). Furthermore, when exposed to PLX5622, *Cb$_2$R*
386 expression was notably lower in 5xFAD/FAAH$^{-/-}$ mice compared to 5xFAD mice.

387

388 **Plaque-associated microglia exhibited greater resistance to PLX5622 compared to non-plaque-**
389 **associated microglia.**

390 We next performed an *in vivo* study of microglial function using multiphoton microscopy. A
391 cranial window was implanted on 5xFAD/Cx3cr1$^{GFP/+}$ and 5xFAD/FAAH$^{-/-}$/Cx3cr1$^{GFP/+}$ mice to
392 perform a longitudinal examination of the microglial response when exposed to PLX5622 (Fig.
393 4A). This approach allowed an in-depth characterization of microglial subtypes in the presence
394 or absence of FAAH activity and under the influence of amyloid-induced neuroinflammation. To
395 test the PLX5622 microglia depleting effect, we chronically imaged the microglia population

396 before PLX5622 treatment initiation (Day 0), after the chronic exposure to the CSF1R-antagonist
397 (Day 28), and after treatment withdrawal and microglial repopulation (Day 37). Images were
398 analyzed using Imaris 10.0 S*pots* tool, and the percentage of living cells relative to day 0 was
399 quantified (Fig. 4B). To perform a detailed follow-up of the microglial response, we differentiated
400 "plaque-associated" cells (located at less than 20 µm from amyloid plaque center) from "non-
401 plaque associated" cells (located >20 µm from the plaque center). These microglial subtypes
402 showed different sensitivity to PLX5622 treatment. Specifically, 69% and 58% of plaque-
403 associated microglia in 5xFAD/Cx3cr1$^{GFP/+}$ and 5xFAD/FAAH$^{-/-}$/Cx3cr1$^{GFP/+}$ mice, respectively,
404 survived after the PLX5622 treatment (Day 28; Fig. 4C and 4E), while 14% and 21% of living cells
405 was observed for non-plaque-associated microglia (Fig. 4E and 4E). FAAH deletion did not cause
406 significant differences in cell survival after 28 days of treatment. At day 37 the glial population
407 was restored to levels of those on day 0 (Fig. 4C and 4D). These results suggest that plaque-
408 associated microglia may be less responsive to PLX5622 treatment than non-plaque-associated
409 microglia, and that both microglial subtypes have similar repopulation rates regardless of FAAH
410 activity under pathological conditions.

411

412 **Exposure to PLX5622 reveals unique morphological features in neuritic plaque-associated**
413 **microglia in FAAH-deficient mice.**

414 We next aimed to characterize microglial morphology changes associated with FAAH genetic
415 inactivation in the context of AD and microglial ablation. To achieve this, we performed a
416 longitudinal imaging study using *in vivo* multiphoton microscopy while administering PLX5622 to
417 5xFAD/Cx3cr1$^{GFP/+}$ and 5xFAD/FAAH$^{-/-}$/Cx3cr1$^{GFP/+}$ mice. Imaging sessions were performed at
418 different time-points and the images obtained after each session were processed and three-
419 dimensionally reconstructed and analyzed using Imaris Software. First, we quantified the
420 number of Sholl intersections of plaque-associated and non-plaque- associated microglia (Fig.

5). At day 0, the Sholl analysis of 5xFAD/FAAH$^{-/-}$/Cx3cr1$^{GFP/+}$ plaque-associated microglia revealed a more complex structure than that of 5xFAD/Cx3cr1$^{GFP/+}$ mice, as observed by the significantly higher number of Sholl intersections (Fig. 5A). This increased microglial complexity was also detected both after exposure to PLX5622 at day 28 (Fig. 5B) as well as after repopulation at day 37 (Fig. 5C). However, neither the genetic inactivation of *Faah* nor PLX5622 exposure affected non-plaque-associated microglial complexity (Fig. 5D, 5E and 5F).

To characterize the morphological features of processes and soma of microglia, images were reconstructed and analyzed using Imaris 10.0 filament and surface tools, respectively (Fig. 6A and 6B). Regarding cell processes of plaque-associated microglia, 5xFAD/Cx3cr1$^{GFP/+}$ mice showed significant morphological changes after PLX5622 treatment, while the glia of 5xFAD/FAAH$^{-/-}$/Cx3cr1$^{GFP/+}$ mice remained almost unaltered (Fig. 6C to E). The glia from 5xFAD/Cx3cr1$^{GFP/+}$ mice exhibited shorter processes (Fig. 6C), with higher sphericity (Fig. 6D), and lower ramification index (Fig. 6E) than those of 5xFAD/FAAH$^{-/-}$/Cx3cr1$^{GFP/+}$ microglia. On the other hand, the volume and soma sphericity of plaque-associated microglia were not significantly affected by PLX5622 treatment (Supplementary Material Fig. S3A). Finally, processes of non-plaque associated microglia were almost unaffected by PLX5622 treatment (Fig. 6F to 6H), while soma showed lower sphericity and higher volume linked to 5xFAD/Cx3cr1$^{GFP/+}$ mice (Supplementary Material Fig. S3B).

PLX5622 treatment revealed changes in phagocytic microglial activity linked to FAAH genetic inactivation that also impacted the progression of neuritic plaques.

Time-lapse analysis of *in vivo* microglial dynamics allowed us to determine the effect of FAAH enzyme inactivation on the phagocytic activity of microglia and on the progression of the amyloid pathology. Microglial phagocytic activity was determined by the presence or absence of methoxy-X04 labelling in microglia and we identified X04-positive microglia as cells with

potential phagocytic role (Fig. 7A). The number of microglial X04-positive cells was quantified and expressed as the percentage of the total number of microglial cells (Fig. 7B). After 28 days of PLX5622 exposure, we observed that *Faah* gene inactivation was associated with a significant increase in the percentage of X04-positive microglial cells (Fig. 7B), suggesting an enhanced phagocytic activity.

We also analyzed several structural features of amyloid plaques (Fig. 7C to H). Our data show that amyloid plaques in 5xFAD/FAAH$^{-/-}$/Cx3cr1$^{GFP/+}$ mice remained almost unaffected by PLX5622 treatment (except for an increase in plaque density at day 28) (Fig. 7F). Plaques in 5xFAD/Cx3cr1$^{GFP/+}$ mice, however, showed larger plaque volume (Fig. 7D) and reduced plaque sphericity (Fig. 7E) than those in 5xFAD/FAAH$^{-/-}$/Cx3cr1$^{GFP/+}$ mice at days 28 and 37. Therefore, we conclude that the lack of FAAH activity resulted in different plaque progression patterns following microglia ablation.

DISCUSSION

Intraneuronal deposits of abnormal tau tangles, reduced levels of acetylcholinesterase, and formation of Aβ-plaques have long been recognized as the primary pathological hallmarks of AD in the brain. Recent evidence suggests the involvement of additional mechanisms of disease to further explain the pathogenesis of AD. Particularly, neuroinflammation has emerged as a critical player in AD progression, together with the identification of AD risk genes associated with innate immune functions, particularly in microglial cells. Regarding the underlying physiology, there is a significant imperative to understand and regulate interactions between the neurons and microglial cells, to develop approaches that may prevent or delay disease's progression (2,31).

In this study, we demonstrate that the chronic increase in endocannabinoid tone in a mouse model of AD is associated with a genetic profile that triggers an exacerbated inflammatory response. Paradoxically, this finding is accompanied by a lower expression of genes associated

with AD development. This modulation may be mediated by changes in the expression of certain microglial genes, as well as by changes in morphology and activity of microglia in the absence of FAAH. Specifically, FAAH-lacking AD mice showed an upregulation of genes involved in several inflammatory signaling pathways and a DAM genetic profile, whereas the expression of genes associated with AD development was downregulated. Furthermore, after 28 days of PLX5622-induced microglial ablation, we observed that plaque-associated, but not non-plaque-associated, microglial cells in 5xFAD/FAAH$^{-/-}$ mice exhibited a more stable morphological profile (including longer, more ramified, and less spherical processes) and an enhanced uptake of Aβ peptides, along with a reduced growth of amyloid plaques compared to those observed in 5xFAD mice. Consequently, our findings seem to show that, although FAAH is not expressed by microglial cells, it may modulate their functions.

Our previously published data, also obtained in 5xFAD and 5xFAD/FAAH$^{-/-}$ mice, pointed that the genetic inhibition of FAAH in the context of AD lead to a pro-inflammatory environment that prevents memory impairment, preserves synaptic plasticity, and decreases amyloid peptide deposition (14–17). This paradoxical association between exacerbated neuroinflammation and neuroprotective effects in the context of *Faah* gene inactivation was confirmed by the transcriptomic analysis performed in the present study. The most interesting results emerged when we analyzed data from GSEA. Hallmark enrichment analysis detected a significant over-expression of genes associated with cellular processes and signaling pathways involved in inflammatory response (Fig. 1D). In contrast, KEGG enrichment analysis showed a significant down-regulation of genes that usually contribute to AD progression (Fig. 1E). Moreover, we have recently reported an overexpression of TREM2 and CTSD phagocytic-related microglial receptors, which was specifically associated to *Faah* deletion in pathological conditions (14). These two genes are commonly associated to the DAM signature and their over-expression indicated the presence of a DAM-enriched microglial population in 5xFAD/FAAH$^{-/-}$ brains. In the present study, we also evaluated the transcriptional signature associated with DAM defined by

Grubman and colleagues (30). We found that these genes were significantly upregulated in 5xFAD/FAAH$^{-/-}$ mice compared to 5xFAD mice (Fig. 1F). This finding supports the presence of a DAM-enriched microglial population in the brains of 5xFAD/FAAH$^{-/-}$ mice, as highlighted in our previous work (14). Consequently, it appears that the induction of the DAM profile has a beneficial impact regarding amyloidosis levels when FAAH is genetically inactivated. However, the contribution of DAM microglia to AD progression is still under investigation. For instance, recent studies have suggested that the progression of neurodegeneration in AD is not directly linked to DAM genes (32). Nonetheless, it is evident that the dysfunction of homeostatic microglia is closely associated with AD progression (32,33).

We analyzed next the expression of specific genes which are related to microglial activation to study possible differences when FAAH is genetically activated. In AD, Aβ induces TLR4 activation in microglia and promotes the activation of NF-κB and the production of pro-inflammatory cytokines, such as IL1β (34). Additionally, NLRP3 inflammasome activation mainly occurs in microglia and leads to the production of several inflammatory cytokines, like IL-1β and IL-1α (32), playing a key role in the development and progression of Aβ-plaque formation (35). Consequently, we measured mRNA levels of *Tlr4, Nlrp3, Il1β*, and *Il1α* in WT and AD mice to check whether *Faah* gene inactivation changes their expression levels. As expected, we detected a general increase in mRNA expression of these genes due to the AD pathology, being the expression of *Nlrp3* and *Il1β* higher in 5xFAD/FAAH$^{-/-}$ mice when compared with 5xFAD mice (Fig. 2B and 2D).

Together with the evaluation of the expression of genes related to microglia activation, we also measured the expression of colony stimulating factor 1 (CSF1L) and its receptor (CSF1R). CSF1R is predominantly expressed on microglia and CSF1L is generally expressed by neurons and astrocytes in the CNS (36,37). Interestingly, CSF-1R signaling and the expression of CSF-1L can be significantly upregulated during inflammation (37). In the homeostatic brain, a baseline level of

CSF1L helps to maintain microglial roles of synaptic pruning, release of neurotrophic factors, and promotion of brain connectivity (37). However, changes in CSF1L secretion from neurons and astrocytes and increases in CSF1R expression have been described in various pathological conditions of the CNS and are considered activating factors for resting microglia (37). Additionally, the up regulation of CSF1R expression has been linked to the DAM profile (4,7). In our study, we found a significant elevation in CSF1R expression (Fig. 2E) and a reduction in CSF1L expression (Fig. 2G) in 5xFAD/FAAH$^{-/-}$ mice compared to 5xFAD mice. Importantly, these changes were concomitant with decreased microgliosis, as indicated by lower levels of Iba1 protein (Fig. 3A). Decreased microgliosis in 5xFAD/FAAH$^{-/-}$ mice has been previously observed by our group by means of Iba1+ cell densitometry (20) and flow cytometry (16). This observation may be linked to the DAM profile exhibited by microglia in 5xFAD/FAAH$^{-/-}$ mice and could also explain the preservation of homeostatic microglial functions observed in these mice, such as hippocampal synaptic plasticity, dendritic spine density and uptake of Aβ (14). Considering our present results, we suggest that neuroinflammation associated to FAAH genetic inactivation is linked to DAM profile development, which involved changes in CSF1R-axis, that could be, at least in part, responsible of the significant amelioration of the pathology detected in 5xFAD/FAAH$^{-/-}$ mice.

To understand the triggering mechanisms and regulatory checkpoints associated with the role of microglia in AD, and additionally as a novel approach to treat neurogenerative diseases, CSF1R inhibitors, such as PLX562, are emerging (6,7). In this way, we also explored whether a pharmacological challenge to microglia could unveil additional features affected by the genetic inactivation of *Faah*. To that end, we employed PLX5622, known to induce a powerful apoptotic response in cells of myeloid origin, including microglia (6). In addition to the expected decrease in microglial markers (TLR4, CSF1R, CB_2) triggered by the administration of PLX5622 (Fig. 3C, 3G y 3H), we also found significant decreases in markers of diverse cellular origin, i.e., IL1α, IL1β, and CSF1L (Fig. 3E, 3F y 3I). Importantly, *Faah* expression levels remained unaltered, confirming

548 that microglial cells exhibit very low expression levels (if any) of this enzyme, as previously
549 described by Muccioli and Stella (38) and that the effects associated to FAAH gene inactivation
550 on microglia observed in this and previous studies (39) reflect a hetero-cellular regulation by
551 other glial and/or neuronal cells.

552 Additionally, the use of PLX5622 allowed us to define and study two different populations of
553 microglia according to their proximity to amyloid plaques: plaque-associated and non-plaque
554 associated microglia. Our study aimed to assess whether the genetic inactivation of *Faah* and
555 the resulting pro-inflammatory environment leads to morphological and *in situ* functional
556 differences in these two populations of microglial cells after their ablation induced by PLX5622
557 and subsequent repopulation. Microglial morphology and changes in plaque-associated
558 microglia have been described as indicators of inflammatory response (40). By using intravital
559 multiphoton microscopy, we observed a surviving microglial population after 28 days of PLX5622
560 exposure and a rapid repopulation after CSF1R inhibition withdrawal (6,41). Our findings
561 revealed that microglia associated with plaques display increased resistance to PLX5622
562 treatment compared to those not associated with plaques (Fig. 4C and 4E). These data agree
563 with those of Spangerberg and collaborators (6), who suggested that the enhanced survival of
564 plaque-associated microglia may be linked to the expression of several markers of the DAM
565 profile in the hippocampus of PLX5622-treated 5xFAD mice, such as CSF1R. In fact, previous
566 works, that also used PLX5622 to cause microglial ablation and analyzed its consequences to AD
567 pathology, described that the Iba1+ cells detected in the brains of PLX5622-treated animals did
568 co-express CSF1R and seem to be resistant to the PLX5622 treatment (42,43). However, further
569 characterization should be required to delineate the precise role of DAM in the progression of
570 neuritic plaques (6).

571 We also analyzed microglial morphology due to its close relation to cellular function (44). Some
572 of the parameters extensively used to assess this analysis are sphericity, volume, length, and

number of end points of microglial processes, among others (45–47). Our results indicate that the lack of *Faah* activity in AD may contribute to increased branching complexity of plaque-associated microglia (Fig. 5A to 5C and Fig. 6C). This complexity remained stable throughout PLX5622 exposure. In contrast, 5xFAD mice exhibited morphological changes typically associated with microglial transition into a more amoeboid state.

Ramified morphology was long thought to be adopted by microglial cells under physiological conditions and were termed as “resting microglia” (48). In contrast, ameboid shape with thickened and retracted processes were traditionally linked to an activation state associated with the enhancement of several glial functions like migration, antigen presentation or phagocytosis (49–51). Nevertheless, this two-state microglial activation paradigm seems now outdated due to the discovery through ultrastructural analysis of alternative microglial phenotypes (52,53). Moreover, *in vivo* two-photon imaging data has revealed that microglia are continuously active in the CNS, being able to phagocytose cellular debris through their terminal branches. It is also generally accepted that ameboid microglia exhibit reduced phagocytic activity (54–58). Therefore, microglia react to different factors such as species, sex, age, specific brain area, and health or disease conditions by transitioning to different states and displaying several functions (59).

Our data indicate that, despite FAAH not being expressed in microglia, the absence of FAAH activity impairs microglial function, which, in turn, triggers significant changes in neuritic plaque structural features. We observed a progressive increase in plaque volume in 5xFAD mice (Fig. 7D), whereas 5xFAD/FAAH$^{-/-}$ mice exhibited an unaltered progression of neuritic plaque volume alongside an increased number of X04+ microglial cells (Fig. 7D and 7B, respectively), despite the more ramified morphology of their plaque-associated microglia. In addition, these mice showed plaques with increased density after PLX5622 exposure (Fig.7F). These observations are in accord with previous reports showing that microglial depletion by CSF1R antagonism leads to increased

plaque size (60,61), and confirm a critical role for microglia in maintaining compact-like plaques, thereby limiting the growth of amyloid plaques and potentially slowing the progression of neuritic dystrophy (62,63). Although the neuroprotective or detrimental role of microglia in AD progression is still a subject of debate (64), FAAH may be considered as a relevant modulator of microglial function, specifically in microglia located near neuritic plaques.

CONCLUSIONS

In the present work, we demonstrate that chronic increase in endocannabinoid tone due to FAAH genetic inactivation in a mouse model of AD leads to a gene expression profile that triggers an exacerbated inflammatory response, which is paradoxically coupled to a lower expression of genes associated with AD development. This modulation seems to be influenced by alterations in the expression of certain microglial genes together with changes in microglial morphology and function following *Faah* gene inactivation. Specifically, our studies revealed an increase in the expression of genes linked to a DAM signature, suggesting an enrichment of this microglial population in 5xFAD/FAAH$^{-/-}$ mice brains. Additionally, after 28 days of pharmacological microglial ablation induced by PLX5622, we observed that plaque-associated microglial cells in 5xFAD/FAAH$^{-/-}$ mice exhibited a more stable morphological profile that enhanced the uptake of Aβ peptides and reduced the growth of amyloid plaques compared to those in 5xFAD mice.

In summary, our findings showed that, although FAAH is not expressed by microglial cells, it may modulate their functions, leading to neuroprotective effects associated, paradoxically, to an exacerbated inflammatory response. Taken together, the present data highlight FAAH as a potential therapeutic target in AD.

LIST OF ABBREVIATIONS

5xFAD: Five familial Alzheimer's disease mutations

Aβ: Amyloid beta

AD: Alzheimer´s Disease

AEA: Anandamide

CB_2R: Cannabinoid receptor subtype 2

CSF1L: Colony stimulating factor 1 ligand

CSF1R: Colony stimulating factor 1 receptor

DAM: Disease-associated microglia

ECS: Endocannabinoid system

FAAH: Fatty acid amide hydrolase

FDR: False Discovery Rate

GSEA: Gene Set Enrichment Analysis

IL1α: Interleukin 1 alpha

IL1β: Interleukin 1 beta

KEGG: Kyoto Encyclopedia of Genes and Genomes

mRNA: Messenger ribonucleic acid

MSigDB: Molecular Signatures Database

NAEs: N-acylethanolamines

NES: Normalized Enrichment Scores

NLRP3: NOD-, LRR- and pyrin domain-containing protein 3

RNA-seq: Ribonucleic acid sequencing

RT-qPCR: Reverse transcription-quantitative polymerase chain reaction

TLR4: Toll-like receptor 4

AUTHORS' CONTRIBUTIONS

JR and AMR designed the experiments; MAA, MF, MTG, SRdME and AMR carried out the experiments; GRP, BJC, RM provided materials; VJSA, JR and AMR wrote the manuscript. All authors revised the final version of the manuscript.

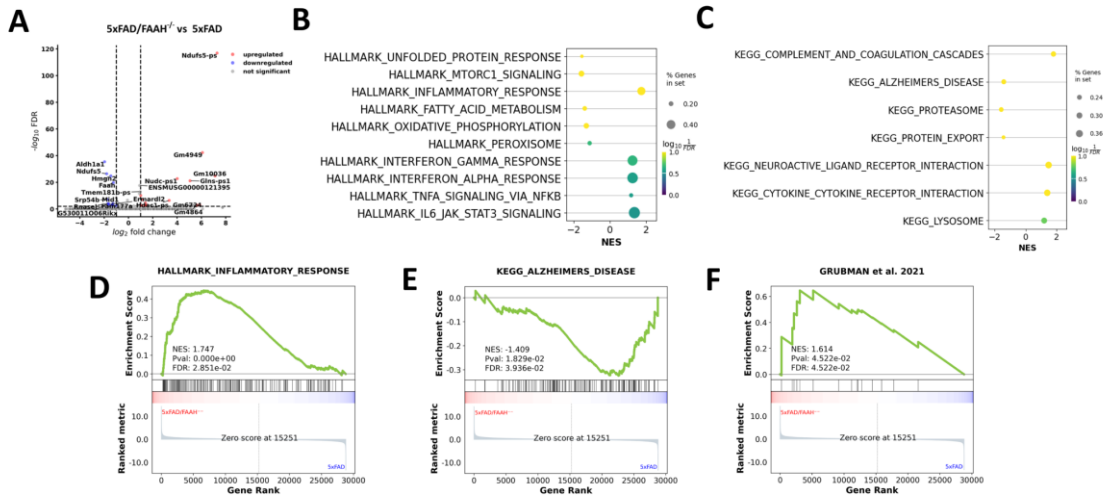

Figure 1: Differential Expression and Pathway Interplay Elicited by FAAH inactivation. (A) Volcano plot representing differential gene expression in 5xFAD/FAAH$^{-/-}$ mice compared to 5xFAD mice (n=3 per genotype), with significant upregulation (red), significant downregulation (blue), and non-significant changes (grey). Notable genes are labelled. **(B)** Hallmark gene set enrichment analysis highlighting the top enriched pathways, with dot size correlating with the percentage of genes involved and color intensity representing FDR significance. **(C)** Enrichment of KEGG pathways shown by NES values; dot size indicates the percentage of genes in the set, and color denotes FDR significance. **(D-F)** GSEA plots for the "Inflammatory Response", "Alzheimer's Disease", and microglia signature from Grubman et al., 2021, respectively, with the x-axis representing gene rank, the y-axis showing the running enrichment score, and vertical lines indicating the position of AD-FAAH within the gene list. The plots illustrate significant pathways with FDR-adjusted p values < 0.05, emphasizing the genes contributing to the enrichment score at the peak of each plot.

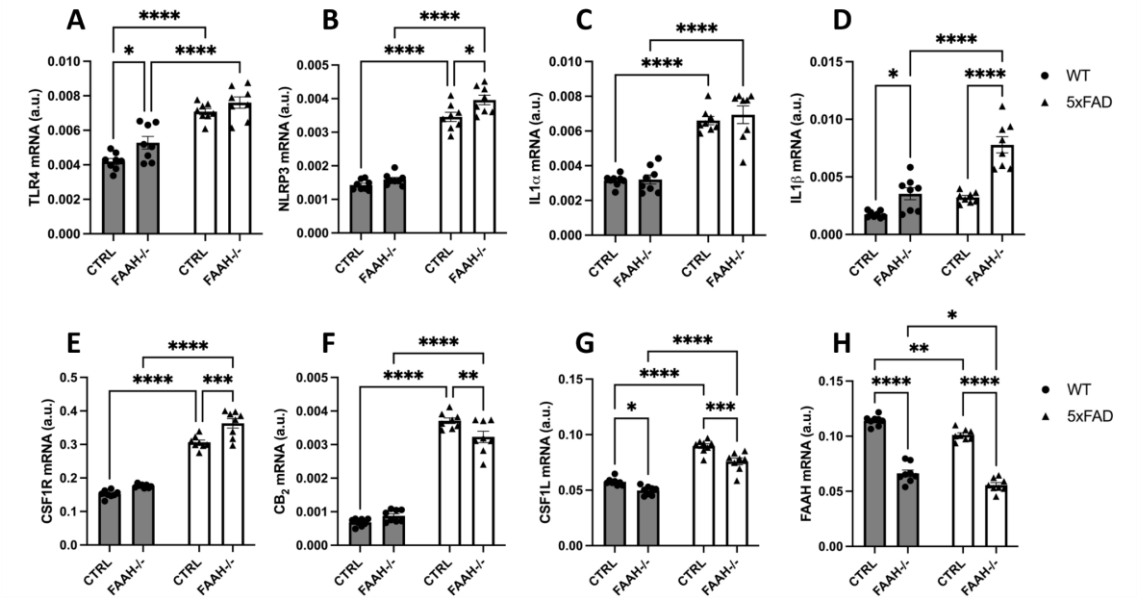

682

683 **Figure 2: Amyloid pathology selectively modifies the expression levels of several key microglial**
684 **genes.** Expression levels of the microglial markers *Tlr4* **(A)**, *Nlrp3* **(B)**, *Il1α* **(C)**, *Il1β* **(D)**, *Csf1r* **(E)**
685 and *Cb₂* **(F)** were increased as a consequence of the enhanced amyloid production characteristic
686 of 5xFAD mice (*p<0.05; **p<0.01; ***p=0.001; ****p<0.0001). *Csf1l* expression levels **(G)**,
687 although of neuronal origin, were also significantly modified due to the pathology (*p<0.05;
688 ***p=0.001; ****p<0.0001). *Faah* expression **(H)** decreased as in 5xFAD mice (*p<0.05;
689 **p<0.01; ****p<0.0001). Data are presented as mean ± standard error of the mean. N=8 mice
690 per group.

691

692

693

694

695

696

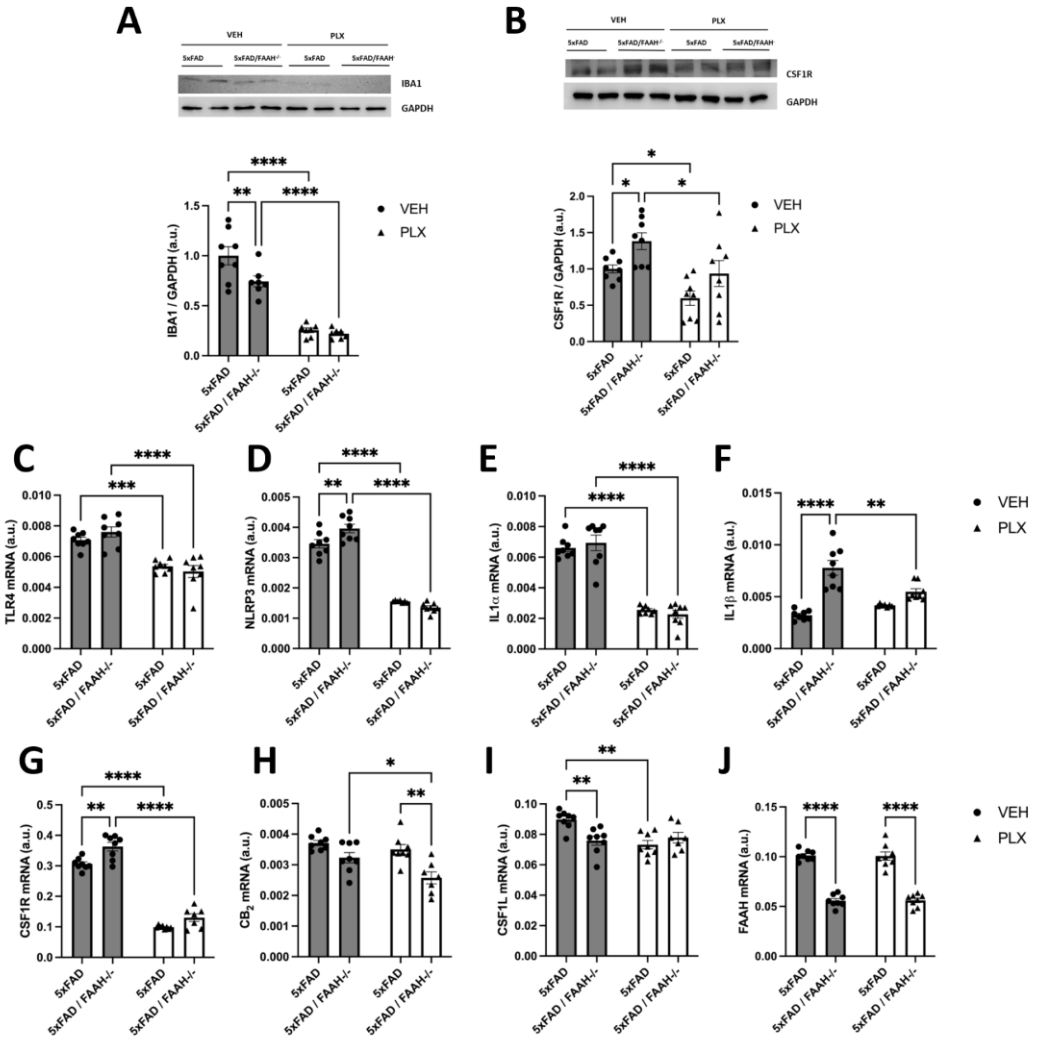

Figure 3: PLX5622 exposure induces the ablation of microglial cells in the brains of 5xFAD mice and significantly reduced the expression levels of microglial markers. (A) IBA1 protein levels were significantly lower in FAAH-lacking AD mice (**p<0.01); Iba1 was significantly diminished after treatment with PLX5622 in both 5xFAD and 5xFAD/FAAH$^{-/-}$ mice (****p<0.0001). **(B)** CSF1R protein levels were increased in FAAH$^{-/-}$ mice and significantly reduced after treatment with PLX5622 (*p<0.05). mRNA levels of *Tlr4* **(C)**, *Nlrp3* **(D)**, *Il1α* **(E)**, *Il1β* **(F)**, and C*sf1r* **(G)** were dramatically reduced after treatment with the CSF1R antagonist, PLX5622 (**p<0.01; ***p=0.001; ****p<0.0001). **(H)** *Cb_2* mRNA levels were diminished in 5xFAD/FAAH$^{-/-}$ but not in 5xFAD mice (*p<0.05; **p<0.01), probably due to the restricted expression of this receptor in plaque-associated microglia, which exhibited significantly higher resistance to PLX5622 treatment (see text). **(I)** The neuronal marker *Csf1l* was also affected by PLX5622 treatment (**p<0.01), but no differences were found between genotypes. **(J)** *Faah* expression was significantly lower in 5xFAD/FAAH$^{-/-}$ mice (****p<0.0001) and remained unaltered after exposure to PLX5622. Data are presented as mean ± standard error of the mean. N=8 mice per group.

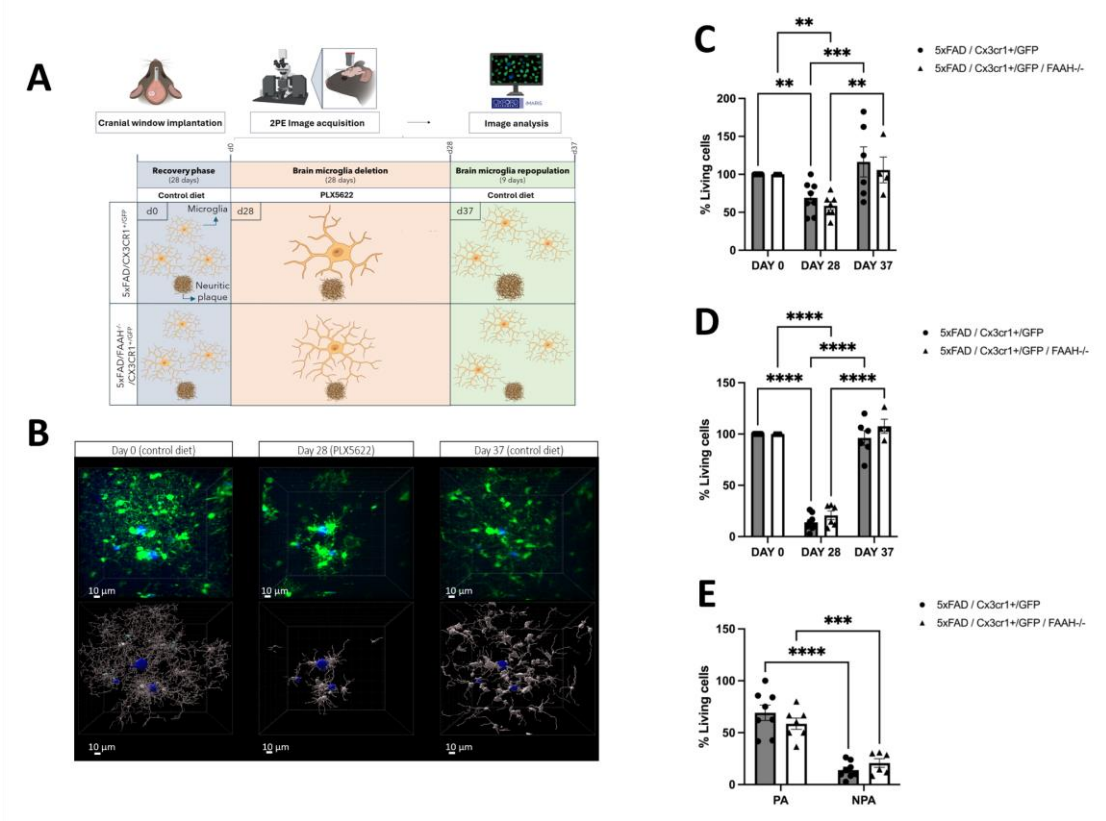

713

714 **Figure 4: PLX5622-induced apoptosis reveals different subpopulations of microglial cells in**
715 **5xFAD mice. (A)** Schematic representation of the experimental set-up performed in the *in vivo*
716 study of microglial function using multiphoton microscopy **(B)** Top: Representative time-lapse *in*
717 *vivo* multiphoton microscopy images of the effect of PLX5622 on microglial survival. After 28 days
718 of exposure to PLX5622 (middle panel) a clear reduction in microglial cell population was evident
719 with respect to day 0 (left panel). Note that this decrease was especially intense in areas located
720 far from neuritic plaques (blue color), while microglial cells surrounding these pathological
721 structures survived. 9 days after the return to normal diet (day 37), a significant re-population
722 was evident (right panel). Bottom: 3D reconstructions of the microscope fields shown. **(C)** Time-
723 course of the ablation and subsequent re-population process of plaque-associated (<20 µm
724 distance from plaque center) microglial cells; % of survival after 28 days of exposure to PLX5622
725 was of 69.16±20.85 and 58.60±14.32 for 5xFAD/Cx3cr1$^{GFP/+}$ and 5xFAD/FAAH$^{-/-}$/Cx3cr1$^{GFP/+}$,
726 respectively. **(D)** Non-plaque associated microglial cells (>20 µm distance from plaque center)
727 survival was of 13.96±8.00 % and 20.70±10.23 % for 5xFAD/Cx3cr1$^{GFP/+}$ and 5xFAD/FAAH$^{-/-}$
728 /Cx3cr1$^{GFP/+}$, respectively. **(E)** The rate of survival of microglial cells was significantly lower in non-
729 plaque associated microglial cells (NPA) than in those located in close vicinity to these
730 pathological structures (plaque-associated cells, PA), independently of the genotype
731 (***p=0.001; ****p<0.0001). Data are presented as mean ± standard error of the mean. N=8-9
732 mice per group.

733

734

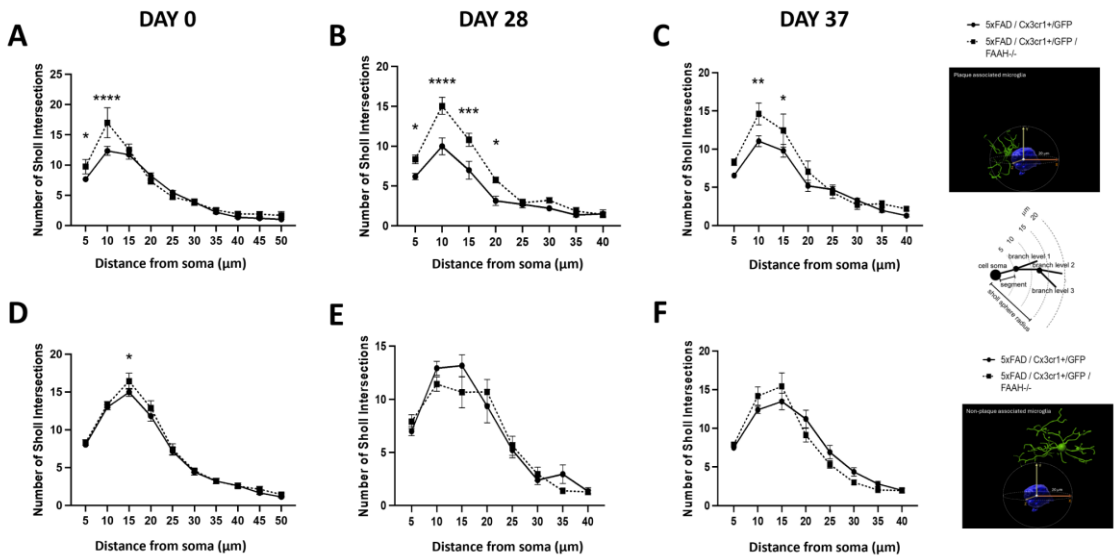

Figure 5: Time-course Sholl analysis of microglial morphological complexity. (A to C) Arborization complexity of plaque-associated 5xFAD/Cx3cr1$^{GFP/+}$ vs. 5xFAD/FAAH$^{-/-}$/Cx3cr1$^{GFP/+}$ microglia before the treatment with PLX5622 (day 0), the last day of treatment (day 28), and 9 days after recovery (day 37); microglia from FAAH-lacking mice exhibited increased complexity at all time points studied (*p<0.05; **p<0.01; ***p=0.001; ****p<0.0001). **(D to F)** Sholl analysis of non-plaque associated microglia revealed no differences between groups at the time points studied in this glial subpopulation. Data are presented as mean ± standard error of the mean. N=8-11 mice per group.

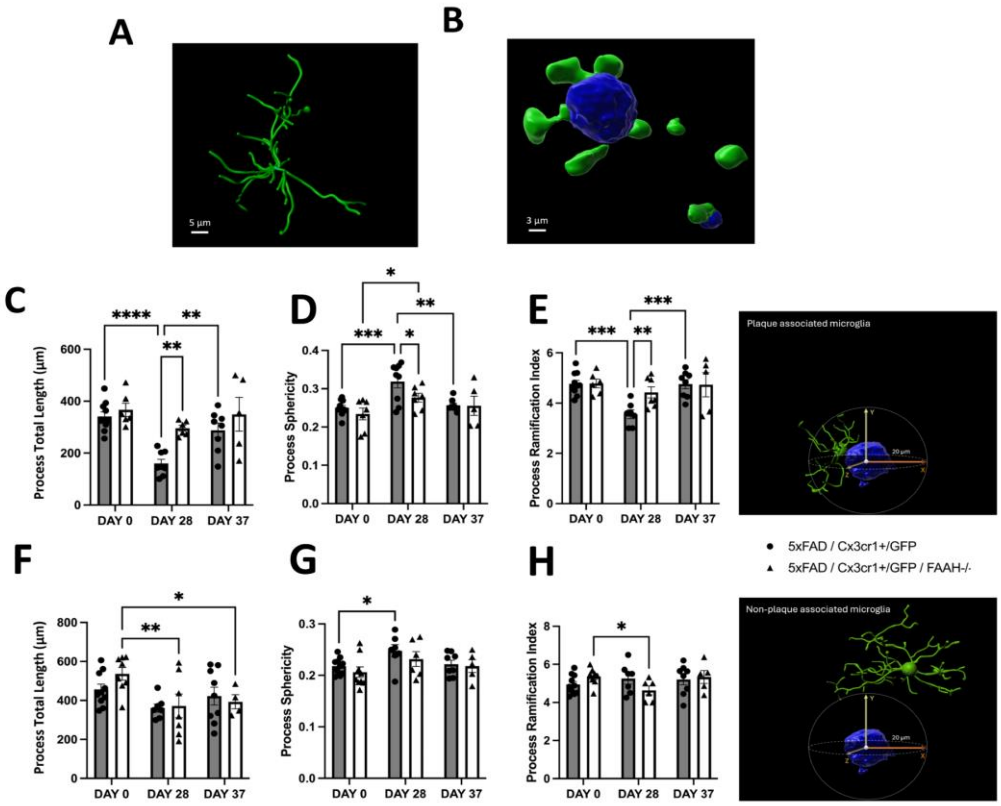

Figure 6: Time-course analysis of processes from plaque and non-plaque associated microglial cells. (A and B) Representative 3D reconstruction (Imaris) of *in vivo* multiphoton images of microglial processes. *Faah* gene inactivation prevented PLX5622-induced changes in morphological features of microglial processes in plaque-associated cells; total length **(C)**, sphericity **(D)**, and ramification index **(E)** were dramatically altered in 5xFAD/Cx3cr1$^{GFP/+}$ mice after 28 days of exposure to PLX5622 and returned to normal levels after 9 days of normal diet. Microglia from 5xFAD/FAAH$^{-/-}$/Cx3cr1$^{GFP/+}$ mice, however, exhibited constant features throughout the period studied (*p<0.05; **p<0.01; ***p=0.001; ****p<0.0001). **(F to H)** Non-plaque associated cells exhibited limited changes after treatment with PLX5622, with no differences due to genotype (*p<0.05; **p<0.01). Data are presented as mean ± standard error of the mean. N=8-11 mice per group.

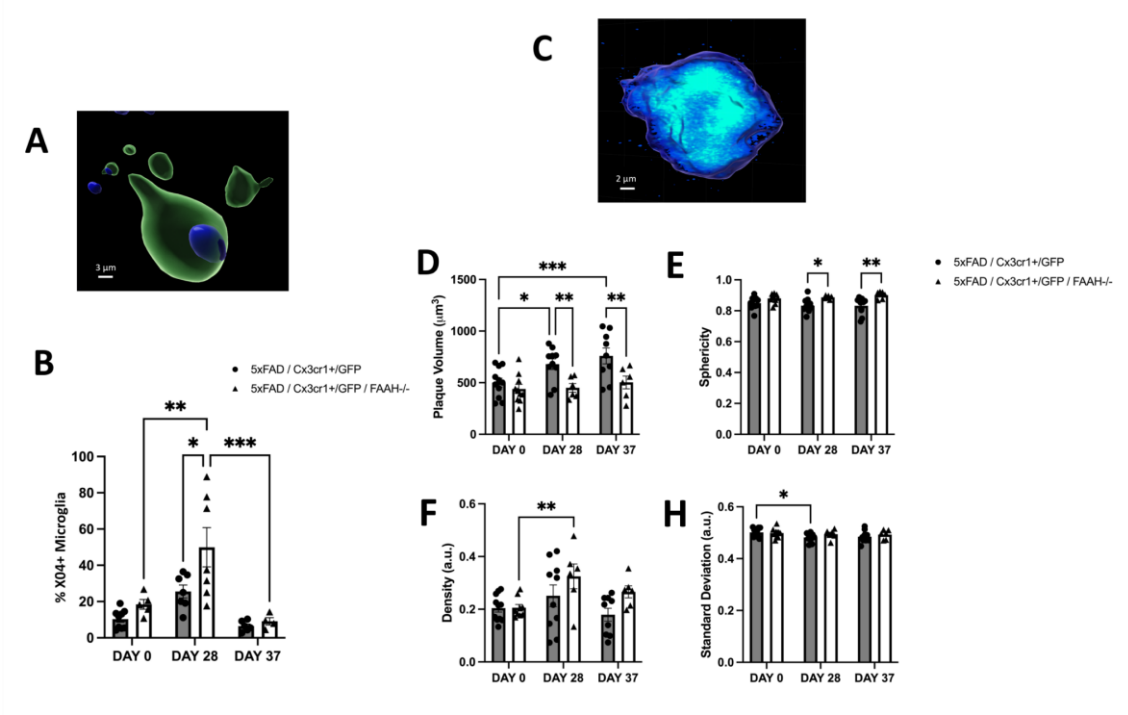

Figure 7: *FAAH* inactivation induced a significant increase in microglial phagocytosis and changes in neuritic plaques features. (A) Representative 3D reconstruction (Imaris) of *in vivo* multiphoton images of microglia-plaque interaction. This approach allowed for the precise observation and quantification of amyloid effectively being phagocytosed (internalized) by microglial cells. In green: microglial soma associated to GFP expression in this mouse model. In blue: amyloid peptide plaque associated to X04 fluorescent signal. **(B)** The percentage of X04-positive microglial was significantly higher in 5xFAD/FAAH$^{-/-}$/Cx3cr1$^{GFP/+}$ than in 5xFAD/Cx3cr1$^{GFP/+}$ mice (*p<0.05; **p<0.01; ***p=0.001). **(C)** Representative 3D reconstruction (Imaris) of a neuritic plaque stained with X04; this approach allowed a detailed description of key structural features of these pathological deposits. An increased fluorescent intensity is associated to a higher concentration of amyloid peptide into the plaque associated to X04 fluorescent signal. **(D to H)** The analysis of amyloid plaques revealed that the *Faah* gene inactivation prevented the increase in plaque volume that was observed in 5xFAD/Cx3cr1$^{GFP/+}$ mice and led to an increased sphericity (*p<0.05; **p<0.01; ***p=0.001). Data are presented as mean ± standard error of the mean. N=8-11 mice per group.

REFERENCES

1. Zhang XX, Tian Y, Wang ZT, Ma YH, Tan L, Yu JT. The Epidemiology of Alzheimer's Disease Modifiable Risk Factors and Prevention. J Prev Alzheimers Dis [Internet]. 2021 Jul 1 [cited 2024 Mar 25];8(3):313–21. Available from: https://pubmed.ncbi.nlm.nih.gov/34101789/

2. Leng F, Edison P. Neuroinflammation and microglial activation in Alzheimer disease: where do we go from here? Vol. 17, Nature Reviews Neurology. 2021.

3. Heneka MT, Carson MJ, Khoury J El, Landreth GE, Brosseron F, Feinstein DL, et al. Neuroinflammation in Alzheimer's disease. Vol. 14, The Lancet Neurology. 2015.

4. Keren-Shaul H, Spinrad A, Weiner A, Matcovitch-Natan O, Dvir-Szternfeld R, Ulland TK, et al. A Unique Microglia Type Associated with Restricting Development of Alzheimer's Disease. Cell. 2017;169(7).

5. Muzio L, Viotti A, Martino G. Microglia in Neuroinflammation and Neurodegeneration: From Understanding to Therapy. Vol. 15, Frontiers in Neuroscience. 2021.

6. Spangenberg E, Severson PL, Hohsfield LA, Crapser J, Zhang J, Burton EA, et al. Sustained microglial depletion with CSF1R inhibitor impairs parenchymal plaque development in an Alzheimer's disease model. Nat Commun. 2019;10(1).

7. Han J, Chitu V, Stanley ER, Wszolek ZK, Karrenbauer VD, Harris RA. Inhibition of colony stimulating factor-1 receptor (CSF-1R) as a potential therapeutic strategy for neurodegenerative diseases: opportunities and challenges. Vol. 79, Cellular and Molecular Life Sciences. 2022.

8. Lu HC, Mackie K. Review of the Endocannabinoid System. Vol. 6, Biological Psychiatry: Cognitive Neuroscience and Neuroimaging. 2021.

9. Lowe H, Toyang N, Steele B, Bryant J, Ngwa W. The endocannabinoid system: A potential target for the treatment of various diseases. Vol. 22, International Journal of Molecular Sciences. 2021.

10. Van Egmond N, Straub VM, Van Der Stelt M. Targeting Endocannabinoid Signaling: FAAH and MAG Lipase Inhibitors. Vol. 61, Annual Review of Pharmacology and Toxicology. 2021.

11. Tripathi RKP. A perspective review on fatty acid amide hydrolase (FAAH) inhibitors as potential therapeutic agents. Vol. 188, European Journal of Medicinal Chemistry. 2020.

12. Jain S, Bisht A, Verma K, Negi S, Paliwal S, Sharma S. The role of fatty acid amide hydrolase enzyme inhibitors in Alzheimer's disease. Vol. 40, Cell Biochemistry and Function. 2022.

13. Papa A, Pasquini S, Contri C, Gemma S, Campiani G, Butini S, et al. Polypharmacological Approaches for CNS Diseases: Focus on Endocannabinoid Degradation Inhibition. Cells. 2022;11(3).

14. Ruiz-Pérez G, Ruiz de Martín Esteban S, Marqués S, Aparicio N, Grande MT, Benito-Cuesta I, et al. Potentiation of amyloid beta phagocytosis and amelioration of synaptic

dysfunction upon FAAH deletion in a mouse model of Alzheimer's disease. J Neuroinflammation. 2021;18(1).

15. Vázquez C, Tolón RM, Pazos MR, Moreno M, Koester EC, Cravatt BF, et al. Endocannabinoids regulate the activity of astrocytic hemichannels and the microglial response against an injury: In vivo studies. Neurobiol Dis. 2015;79.

16. Aparicio N, Grande MT, Ruiz de Martín Esteban S, López A, Ruiz-Pérez G, Amores M, et al. Role of interleukin 1-beta in the inflammatory response in a fatty acid amide hydrolase-knockout mouse model of Alzheimer's disease. Biochem Pharmacol. 2018;157.

17. Benito C, Núñez E, Tolón RM, Carrier EJ, Rábano A, Hillard CJ, et al. Cannabinoid CB2 Receptors and Fatty Acid Amide Hydrolase Are Selectively Overexpressed in Neuritic Plaque-Associated Glia in Alzheimer's Disease Brains. Journal of Neuroscience. 2003;23(35).

18. Tsou K, Nogueron MI, Muthian S, Sañudo-Peña MC, Hillard CJ, Deutsch DG, et al. Fatty acid amide hydrolase is located preferentially in large neurons in the rat central nervous system as revealed by immunohistochemistry. Neurosci Lett. 1998;254(3).

19. Romero J, Hillard CJ, Calero M, Rábano A. Fatty acid amide hydrolase localization in the human central nervous system: An immunohistochemical study. Molecular Brain Research. 2002;100(1–2).

20. Vázquez C, Tolón RM, Grande MT, Caraza M, Moreno M, Koester EC, et al. Endocannabinoid regulation of amyloid-induced neuroinflammation. Neurobiol Aging. 2015;36(11).

21. Oakley H, Cole SL, Logan S, Maus E, Shao P, Craft J, et al. Intraneuronal β-amyloid aggregates, neurodegeneration, and neuron loss in transgenic mice with five familial Alzheimer's disease mutations: Potential factors in amyloid plaque formation. Journal of Neuroscience. 2006;26(40).

22. Cravatt BF, Demarest K, Patricelli MP, Bracey MH, Giang DK, Martin BR, et al. Supersensitivity to anandamide and enhanced endogenous cannabinoid signaling in mice lacking fatty acid amide hydrolase. Proc Natl Acad Sci U S A. 2001;98(16).

23. Jung S, Aliberti J, Graemmel P, Sunshine MJ, Kreutzberg GW, Sher A, et al. Analysis of Fractalkine Receptor CX 3 CR1 Function by Targeted Deletion and Green Fluorescent Protein Reporter Gene Insertion . Mol Cell Biol. 2000;20(11).

24. Dobin A, Davis CA, Schlesinger F, Drenkow J, Zaleski C, Jha S, et al. STAR: Ultrafast universal RNA-seq aligner. Bioinformatics. 2013;29(1).

25. Liao Y, Smyth GK, Shi W. The R package Rsubread is easier, faster, cheaper and better for alignment and quantification of RNA sequencing reads. Nucleic Acids Res. 2019;47(8).

26. Love MI, Huber W, Anders S. Moderated estimation of fold change and dispersion for RNA-seq data with DESeq2. Genome Biol. 2014;15(12).

27. Fang Z, Liu X, Peltz G. GSEApy: a comprehensive package for performing gene set enrichment analysis in Python. Bioinformatics. 2023;39(1).

28. Subramanian A, Tamayo P, Mootha VK, Mukherjee S, Ebert BL, Gillette MA, et al. Gene set enrichment analysis: A knowledge-based approach for interpreting genome-wide expression profiles. Proc Natl Acad Sci U S A. 2005;102(43).

29. Mostany R, Portera-Cailliau C. A craniotomy surgery procedure for chronic brain imaging. Journal of Visualized Experiments. 2008;(12).

30. Grubman A, Choo XY, Chew G, Ouyang JF, Sun G, Croft NP, et al. Transcriptional signature in microglia associated with Aβ plaque phagocytosis. Nat Commun. 2021;12(1).

31. Kiraly M, Foss JF, Giordano T. Neuroinflammation, Its Role in Alzheimer's Disease and Therapeutic Strategies. J Prev Alzheimers Dis. 2023;10(4):686–98.

32. Sobue A, Komine O, Yamanaka K. Neuroinflammation in Alzheimer's disease: microglial signature and their relevance to disease. Vol. 43, Inflammation and Regeneration. 2023.

33. Holtman IR, Raj DD, Miller JA, Schaafsma W, Yin Z, Brouwer N, et al. Induction of a common microglia gene expression signature by aging and neurodegenerative conditions: a co-expression meta-analysis. Acta Neuropathol Commun. 2015;3.

34. Wu L, Xian X, Xu G, Tan Z, Dong F, Zhang M, et al. Toll-Like Receptor 4: A Promising Therapeutic Target for Alzheimer's Disease. Vol. 2022, Mediators of Inflammation. 2022.

35. Hanslik KL, Ulland TK. The Role of Microglia and the Nlrp3 Inflammasome in Alzheimer's Disease. Vol. 11, Frontiers in Neurology. 2020.

36. Easley-Neal C, Foreman O, Sharma N, Zarrin AA, Weimer RM. CSF1R Ligands IL-34 and CSF1 Are Differentially Required for Microglia Development and Maintenance in White and Gray Matter Brain Regions. Front Immunol. 2019;10.

37. Bo L, Bo X. Colony stimulating factor 1: friend or foe of neurons? Vol. 17, Neural Regeneration Research. 2022.

38. Muccioli GG, Stella N. Microglia produce and hydrolyze palmitoylethanolamide. Neuropharmacology. 2008;54(1).

39. Ativie F, Albayram O, Bach K, Pradier B, Zimmer A, Bilkei-Gorzo A. Enhanced microglial activity in FAAH-/- animals. Life Sci. 2015;138.

40. Kwon HS, Koh SH. Neuroinflammation in neurodegenerative disorders: the roles of microglia and astrocytes. Vol. 9, Translational Neurodegeneration. 2020.

41. Elmore MRP, Hohsfield LA, Kramár EA, Soreq L, Lee RJ, Pham ST, et al. Replacement of microglia in the aged brain reverses cognitive, synaptic, and neuronal deficits in mice. Aging Cell. 2018;17(6).

42. Spangenberg EE, Lee RJ, Najafi AR, Rice RA, Elmore MRP, Blurton-Jones M, et al. Eliminating microglia in Alzheimer's mice prevents neuronal loss without modulating amyloid-β pathology. Brain. 2016;139(4).

43. Unger MS, Schernthaner P, Marschallinger J, Mrowetz H, Aigner L. Microglia prevent peripheral immune cell invasion and promote an anti-inflammatory environment in the brain of APP-PS1 transgenic mice. J Neuroinflammation. 2018;15(1).

44. Lier J, Streit WJ, Bechmann I. Beyond activation: Characterizing microglial functional phenotypes. Vol. 10, Cells. 2021.

45. Torres-Platas SG, Comeau S, Rachalski A, Bo GD, Cruceanu C, Turecki G, et al. Morphometric characterization of microglial phenotypes in human cerebral cortex. J Neuroinflammation. 2014;11.

46. Zhou K, Han J, Lund H, Boggavarapu NR, Lauschke VM, Goto S, et al. An overlooked subset of Cx3cr1 wt/wt microglia in the Cx3cr1 CreER-Eyfp/wt mouse has a repopulation advantage over Cx3cr1 CreER-Eyfp/wt microglia following microglial depletion. J Neuroinflammation. 2022;19(1).

47. Vidal-Itriago A, Radford RAW, Aramideh JA, Maurel C, Scherer NM, Don EK, et al. Microglia morphophysiological diversity and its implications for the CNS. Vol. 13, Frontiers in Immunology. 2022.

48. Wendimu MY, Hooks SB. Microglia Phenotypes in Aging and Neurodegenerative Diseases. Vol. 11, Cells. 2022.

49. Parakalan R, Jiang B, Nimmi B, Janani M, Jayapal M, Lu J, et al. Transcriptome analysis of amoeboid and ramified microglia isolated from the corpus callosum of rat brain. BMC Neurosci. 2012;13(1).

50. Madore C, Joffre C, Delpech JC, De Smedt-Peyrusse V, Aubert A, Coste L, et al. Early morphofunctional plasticity of microglia in response to acute lipopolysaccharide. Brain Behav Immun. 2013;34.

51. Kaur C, Ling EA, Wong WC. Transformation of Amoeboid Microglial Cells into Microglia in the Corpus Callosum of the Postnatal Rat Brain. An Electron Microscopical Study. Archivum histologicum japonicum. 1985;48(1).

52. Sierra A, de Castro F, del Río-Hortega J, Rafael Iglesias-Rozas J, Garrosa M, Kettenmann H. The “Big-Bang” for modern glial biology: Translation and comments on Pío del Río-Hortega 1919 series of papers on microglia. Glia. 2016;64(11).

53. Savage JC, Picard K, González-Ibáñez F, Tremblay MÉ. A brief history of microglial ultrastructure: Distinctive features, phenotypes, and functions discovered over the past 60 years by electron microscopy. Vol. 9, Frontiers in Immunology. 2018.

54. Nimmerjahn A, Kirchhoff F, Helmchen F. Neuroscience: Resting microglial cells are highly dynamic surveillants of brain parenchyma in vivo. Science (1979). 2005;308(5726).

55. Davalos D, Grutzendler J, Yang G, Kim J V., Zuo Y, Jung S, et al. ATP mediates rapid microglial response to local brain injury in vivo. Nat Neurosci. 2005;8(6).

56. Sierra A, Encinas JM, Deudero JJP, Chancey JH, Enikolopov G, Overstreet-Wadiche LS, et al. Microglia shape adult hippocampal neurogenesis through apoptosis-coupled phagocytosis. Cell Stem Cell. 2010;7(4).

57. VanRyzin JW, Marquardt AE, Argue KJ, Vecchiarelli HA, Ashton SE, Arambula SE, et al. Microglial Phagocytosis of Newborn Cells Is Induced by Endocannabinoids and Sculpts Sex Differences in Juvenile Rat Social Play. Neuron. 2019;102(2).

58. Abiega O, Beccari S, Diaz-Aparicio I, Nadjar A, Layé S, Leyrolle Q, et al. Neuronal Hyperactivity Disturbs ATP Microgradients, Impairs Microglial Motility, and Reduces Phagocytic Receptor Expression Triggering Apoptosis/Microglial Phagocytosis Uncoupling. PLoS Biol. 2016;14(5).

59. Paolicelli RC, Sierra A, Stevens B, Tremblay ME, Aguzzi A, Ajami B, et al. Microglia states and nomenclature: A field at its crossroads. Vol. 110, Neuron. 2022.

60. Deczkowska A, Keren-Shaul H, Weiner A, Colonna M, Schwartz M, Amit I. Disease-Associated Microglia: A Universal Immune Sensor of Neurodegeneration. Vol. 173, Cell. 2018.

61. Clayton K, Delpech JC, Herron S, Iwahara N, Ericsson M, Saito T, et al. Plaque associated microglia hyper-secrete extracellular vesicles and accelerate tau propagation in a humanized APP mouse model. Mol Neurodegener. 2021;16(1).

62. Kiani Shabestari S, Morabito S, Danhash EP, McQuade A, Sanchez JR, Miyoshi E, et al. Absence of microglia promotes diverse pathologies and early lethality in Alzheimer's disease mice. Cell Rep. 2022;39(11).

63. Zhao R, Hu W, Tsai J, Li W, Gan WB. Microglia limit the expansion of β-amyloid plaques in a mouse model of Alzheimer's disease. Mol Neurodegener. 2017;12(1).

64. Casali BT, MacPherson KP, Reed-Geaghan EG, Landreth GE. Microglia depletion rapidly and reversibly alters amyloid pathology by modification of plaque compaction and morphologies. Neurobiol Dis. 2020;142.

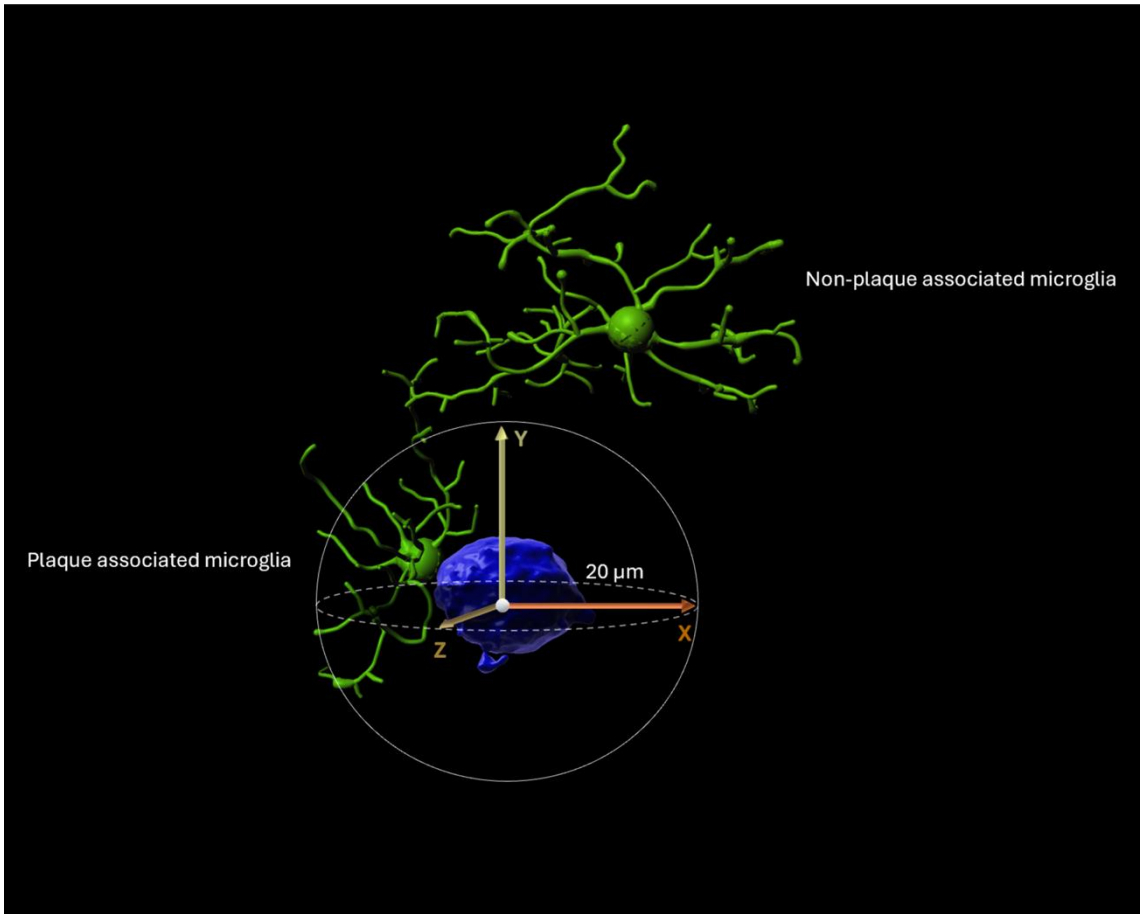

Figure S1: Representative 3D reconstruction of plaque-associated and non-plaque associated microglia. *In vivo* two-photon microscopy images of microglia and amyloid plaques were reconstructed by using the Surface tool of Imaris Software. Microglial soma located less than 20 µm from amyloid plaques were classified as plaque-associated microglia, while those situated further than 20 µm were referred to as non-plaque-associated microglia.

Surface 1 (Microglial soma)	Filaments (Microglial proccesses)
[Algorithm] Enable Region Of Interest = false Enable Region Growing = true Enable Tracking = false Enable Classify = true Enable Shortest Distance = true [Source Channel] Source Channel Index = 2 Enable Smooth = true Surface Grain Size= 0,700 µm Enable Eliminate Background = true Diameter Of Largest Sphere = 7,00 µm [Threshold] Active Threshold = true Enable Automatic Threshold = true Active Threshold B = false Region Growing Estimated Diameter = 7,50 µm Region Growing Morphological Split = false [Filter Seed Points] "Quality" above 370 [Filter Surfaces] "Distance to Image Border XYZ Img=1" above 10,0 µm	[Algorithm] Name = Autopath (no loops) Segment Start Point = true Detect Spines = false Enable Regions Of Interest = false Track (over time) = false [Soma Starting Points] Segment Channel Index = 2 Segment Starting Point Diameter = 7,00 µm Calculate Soma Model = false [Filter Starting Points] Segment Starting Point Threshold Low = 414.951 Segment Starting Point Threshold High = Automatic [Seed Points for Segments] Segment Seed Point Diameter = 1,00 µm [Filter Seed Points for Segments] Segment Seed Point Threshold = 355.343 Diameter around Starting Point(s) to remove Seed Points = 20,0 µm Segment Diameter Filter Strengthness = 2
Surface 2 (Amyloid plaque for microglial localization)	**Surface 3 (Amyloid plaque characterization)**
[Algorithm] Enable Region Of Interest = false Enable Region Growing = false Enable Tracking = false Enable Classify = true Enable Shortest Distance = true [Source Channel] Source Channel Index = 1 Enable Smooth = true Surface Grain Size= 0,700 µm Enable Eliminate Background = false [Threshold] Active Threshold = true Enable Automatic Threshold = false Manual Threshold Value = 46 Active Threshold B = false [Filter Surfaces] "Volume" above 58,0 µm^3	[Algorithm] Enable Region Of Interest = false Enable Region Growing = false Enable Tracking = false Enable Classify = true Enable Shortest Distance = false [Source Channel] Source Channel Index = 1 Enable Smooth = true Surface Grain Size= 0,360 µm Enable Eliminate Background = false [Threshold] Active Threshold = true Enable Automatic Threshold = true Active Threshold B = false [Filter Surfaces] "Volume" above 760 µm^3
Spots (Microglial cell number)	
[Algorithm] Enable Region Of Interest = false Enable Region Growing = false Enable Tracking = false Enable Classify = true Enable Region Growing = false Enable Shortest Distance = true [Source Channel] Source Channel Index = 2 Estimated Diameter = 7,50 µm Background Subtraction = true [Filter Spots] "Quality" above 327	

Figure S2: Imaris Algorithms for segmentation. Imaris algorithms for rendering of microglia soma (Surface 1), microglial processes (Filaments), amyloid plaque for microglial localization (Surface 2), and amyloid plaque (Surface 3), and for counting of microglial cell number (Spots).

1002 **Table S3**. **PyDESeq2 top ranking differentially expressed genes.**

Gene Name	baseMean	log2FoldChange	lfcSE	stat	pvalue	padj
Ndufs5-ps	726.2169348	7.291843218	0.310391414	23.4924128	4.8763E-122	1.4091E-117
Gm4949	189.9865446	6.087672529	0.422177126	14.41971191	3.88963E-47	5.62012E-43
Aldh1a1	1116.4223	-1.965812646	0.148316019	-13.25421665	4.26548E-40	4.10879E-36
Ndufs5	1372.362939	-1.790664745	0.154756854	-11.57082673	5.79218E-31	4.18456E-27
Gm10036	143.1931454	7.127591928	0.634612306	11.23141146	2.85875E-29	1.65224E-25
Hmgn2	1221.373415	-1.447733327	0.129122183	-11.21211935	3.55576E-29	1.71257E-25
Nudc-ps1	88.13660479	4.01413735	0.372631753	10.77239747	4.64739E-27	1.91858E-23
Glns-ps1	406.1809629	5.066900771	0.486780054	10.40901477	2.25544E-25	8.1472E-22
Faah	5418.036665	-1.238558476	0.122789916	-10.08680935	6.31901E-24	2.02896E-20
ENSMUSG00000121395	3442.550199	0.916377027	0.09555697	9.589850185	8.8213E-22	2.54918E-18
Tmem181b-ps	1725.269962	0.971876503	0.115528351	8.412450246	4.01533E-17	1.05486E-13
Ndn	6216.053306	0.89941256	0.112584519	7.988776475	1.36285E-15	3.28196E-12
Col16a1	1844.084168	1.008018354	0.133294821	7.562321985	3.95937E-14	8.80137E-11
Srp54b	196.8896139	-1.725432671	0.260663071	-6.619398237	3.60664E-11	7.44462E-08
Wdfy1	882.8590174	1.146098377	0.174874646	6.553828141	5.60805E-11	1.08041E-07
Cbx6	17430.65147	-0.081515436	0.012720836	-6.408024922	1.47417E-10	2.66253E-07
Hdac1-ps	39.27294482	3.348958866	0.529322082	6.32688297	2.50163E-10	4.25248E-07
Npl	208.1886067	1.397273615	0.248169455	5.630320689	1.79875E-08	2.88779E-05
Dcdc2b	499.8336106	-0.786342564	0.14397978	-5.461479115	4.72184E-08	7.18167E-05
Mid1	216.0589809	-1.271754578	0.233987587	-5.435136942	5.47544E-08	7.91146E-05
Rnasel	188.1464865	-1.62713368	0.300778918	-5.409733133	6.31187E-08	8.68574E-05
G530011O06Rikx	74.93618786	-1.694305447	0.317167254	-5.341993624	9.19299E-08	0.000120754
Ermardl2	77.61282778	-1.625177733	0.319497907	-5.086661593	3.64421E-07	0.000457872
Fam177a	173.8219821	-1.336582179	0.26634476	-5.018240944	5.21468E-07	0.00062789
Fam177a2	173.6677931	-1.334782678	0.266671335	-5.005347419	5.57614E-07	0.000644557
Gm6724	20.04008854	5.870520747	1.198769208	4.897123407	9.72498E-07	0.001080894
Gm43305	217.8824472	1.465140803	0.302228575	4.847790469	1.24844E-06	0.001336202
Gm4864	17.34897685	5.652475287	1.172577692	4.820555028	1.43159E-06	0.001477507
Tmem181c-ps	433.1371198	1.058490906	0.225341593	4.697272675	2.63658E-06	0.00262731
ENSMUSG00000095041	9974.306257	0.750433094	0.160285806	4.681843725	2.84306E-06	0.002738627
Ttc39aos1	107.7724834	1.398475747	0.299597522	4.667848183	3.04371E-06	0.002837324
Slc30a2	169.4478122	-1.009364931	0.220332921	-4.581089949	4.62559E-06	0.004177195
Marcksl1	3146.400613	0.43803678	0.095834995	4.57073933	4.86007E-06	0.004255944
Ccn2	163.5501258	1.298856043	0.288958258	4.494960795	6.95828E-06	0.005836457
Map3k6	88.19251543	-1.349526373	0.300455305	-4.49160441	7.06886E-06	0.005836457
Glul	45443.18936	-0.582866087	0.130099909	-4.48014216	7.45933E-06	0.005987773
Phactr4	460.522055	0.649102778	0.147815007	4.391318523	1.12665E-05	0.008799468
3300002P13Rik	2332.155871	-0.489390094	0.112114554	-4.365089774	1.27071E-05	0.009663382
Iqcc	637.6521909	-0.553035906	0.12748211	-4.338145206	1.4369E-05	0.010647076
Hspa5	8590.209162	-0.456257091	0.10968816	-4.159583777	3.18828E-05	0.022471935
Spocd1	55.99579367	1.608933547	0.386655975	4.161150095	3.16649E-05	0.022471935
Chrm4	405.7792202	0.755092369	0.185025926	4.081008465	4.48407E-05	0.030852552
Colgalt2	292.3102586	0.812514602	0.200067592	4.061200486	4.8821E-05	0.032809998

Med8	581.1122277	-0.561374285	0.139272436	-4.030763746	5.55959E-05	0.036513874
Srp54a	293.9746163	-0.878987611	0.219830661	-3.998475958	6.37517E-05	0.040939896
Agbl4	342.8297762	0.773784578	0.194513928	3.978042007	6.94851E-05	0.043651747
Fam167b	63.36973581	1.51742596	0.383984452	3.951790106	7.75688E-05	0.047693236
Cnih2	16394.4321	-0.379070281	0.096714235	-3.919487961	8.87373E-05	0.053423548
Ncf2-rs	20.28550215	7.742825581	2.003254721	3.865122843	0.000111033	0.064172807
Ncf2-rs	20.28550215	7.742825581	2.003254721	3.865122843	0.000111033	0.064172807

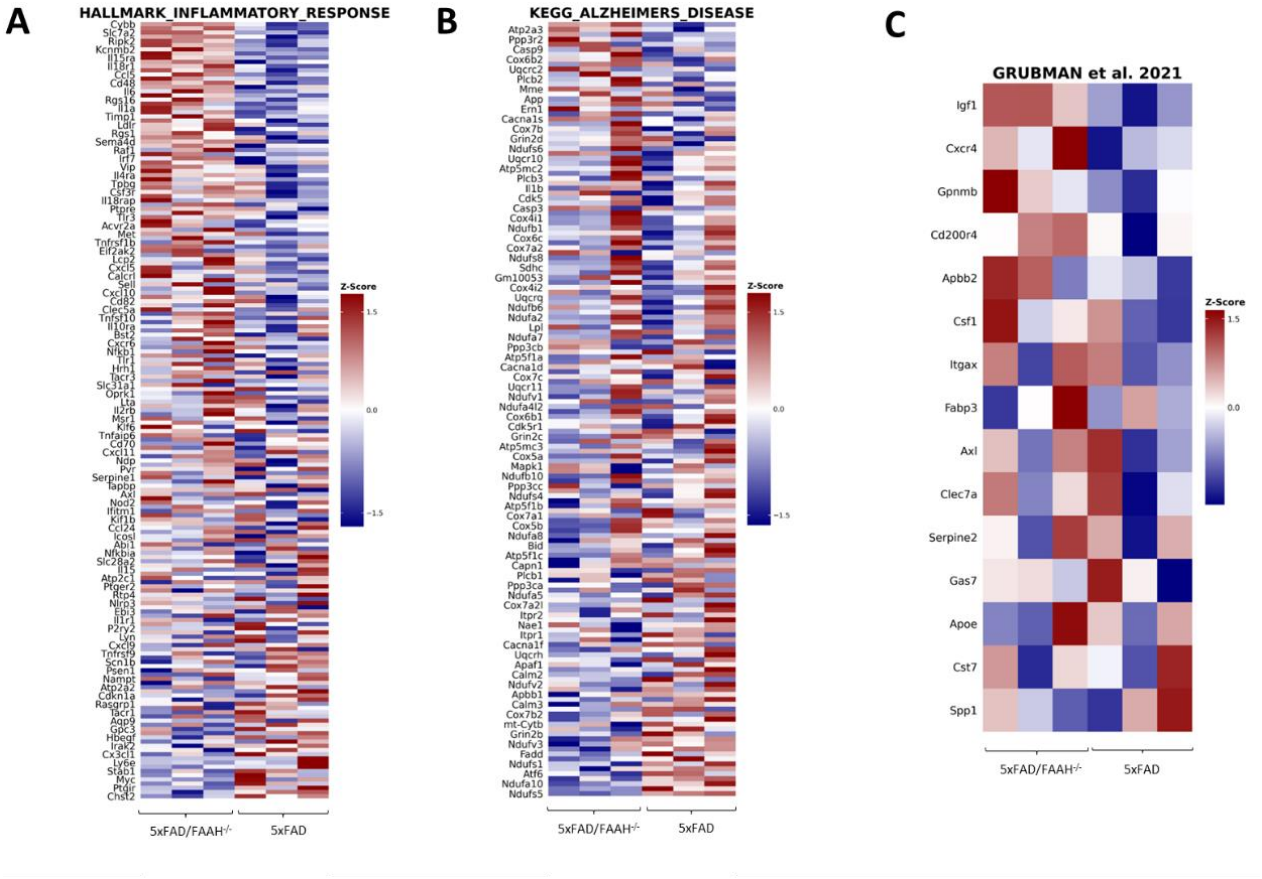

Fig S4: Heatmaps showing Z-score of normalized gene counts in the hippocampi of 5xFAD/FAAH$^{-/-}$ and 5xFAD mouse. Normalized expression levels (Z-score) of genes included in GSEA plots for the "Inflammatory Response" **(A)**, "Alzheimer's Disease" **(B)**, and "Microglia signature from Grubman et al., 2021" **(C)**.

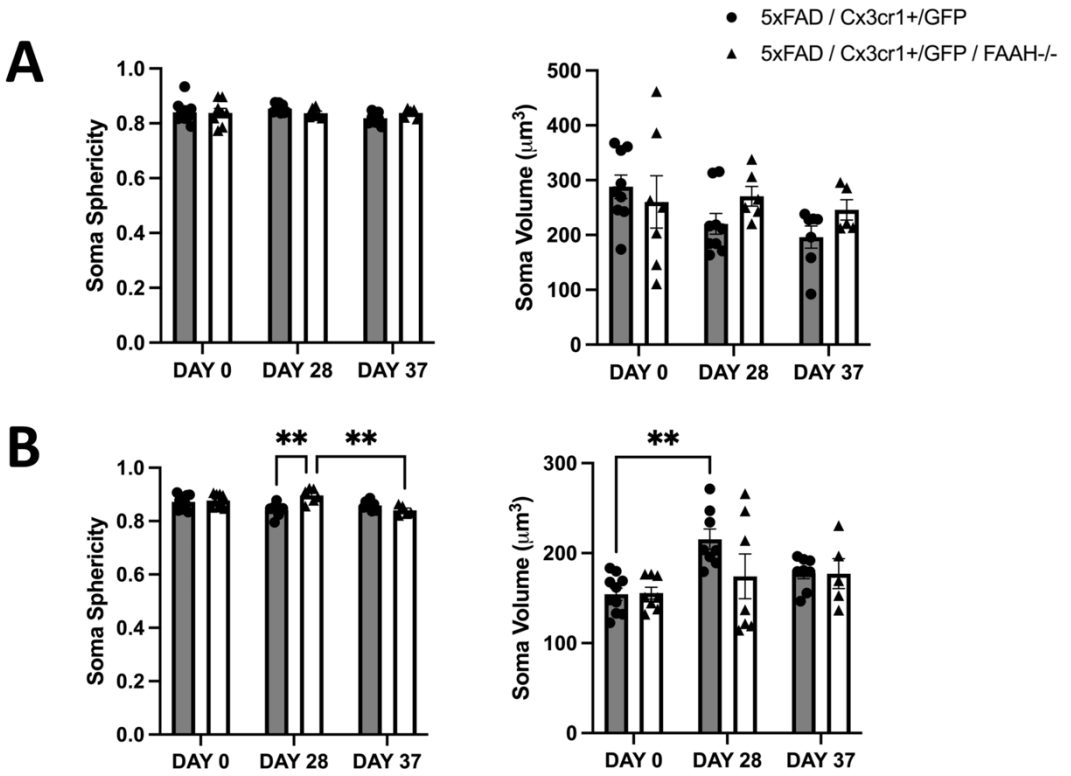

Figure S5: Time-course analysis of cell somas from plaque and non-plaque associated microglial cells. (A) *FAAH* gene inactivation did not modify the structural features (sphericity and volume) of cell somas in plaque-associated microglia. **(B)** Non-plaque associated cells exhibited increased cell soma sphericity on day 28 of treatment due to the gene inactivation of FAAH with no changes in volume linked to the genotype (**p<0.01). Data are presented as mean ± standard error of the mean. N=8-11 mice per group.